

Micro-Chemical Monopropellant Thruster

Contract Number: 043022

Final Report

Sarah Barley

S.Barley@surrey.ac.uk

Supervisor: Dr P Palmer

Surrey Space Centre

University of Surrey

Guildford

Surrey

GU2 7XH



February 2006

Report Documentation Page			Form Approved OMB No. 0704-0188		
Public reporting burden for the collection of information is estimated to average 1 hour per response, including the time for reviewing instructions, searching existing data sources, gathering and maintaining the data needed, and completing and reviewing the collection of information. Send comments regarding this burden estimate or any other aspect of this collection of information, including suggestions for reducing this burden, to Washington Headquarters Services, Directorate for Information Operations and Reports, 1215 Jefferson Davis Highway, Suite 1204, Arlington VA 22202-4302. Respondents should be aware that notwithstanding any other provision of law, no person shall be subject to a penalty for failing to comply with a collection of information if it does not display a currently valid OMB control number.					
1. REPORT DATE 01 FEB 2006		2. REPORT TYPE N/A		3. DATES COVERED 01Aug 2004 - 01 Feb 2006	
4. TITLE AND SUBTITLE Micro-Chemical Monopropellant Thruster			5a. CONTRACT NUMBER FA8655-04-1-3022		
			5b. GRANT NUMBER		
			5c. PROGRAM ELEMENT NUMBER		
6. AUTHOR(S)			5d. PROJECT NUMBER		
			5e. TASK NUMBER		
			5f. WORK UNIT NUMBER		
7. PERFORMING ORGANIZATION NAME(S) AND ADDRESS(ES) University of Surrey Guildford Surrey GU2 7XH United Kingdom			8. PERFORMING ORGANIZATION REPORT NUMBER		
9. SPONSORING/MONITORING AGENCY NAME(S) AND ADDRESS(ES) EOARD PSC 821 Box 14 FPO 09421-0014			10. SPONSOR/MONITOR'S ACRONYM(S)		
			11. SPONSOR/MONITOR'S REPORT NUMBER(S) SPC 04-3022		
12. DISTRIBUTION/AVAILABILITY STATEMENT Approved for public release, distribution unlimited					
13. SUPPLEMENTARY NOTES The original document contains color images.					
14. ABSTRACT					
15. SUBJECT TERMS					
16. SECURITY CLASSIFICATION OF:			17. LIMITATION OF ABSTRACT UU	18. NUMBER OF PAGES 66	19a. NAME OF RESPONSIBLE PERSON
a. REPORT unclassified	b. ABSTRACT unclassified	c. THIS PAGE unclassified			

Executive Summary

This report summarises the work completed under EOARD contract 043022 “Micro-Chemical Monopropellant Thruster”. The research was carried out at the Surrey Space Centre, University of Surrey and the testing was conducted at the Surrey Satellite Technology Ltd Propulsion Test Site, Westcott, Bucks.

The need to extend the on-orbit capabilities of nanosatellites has led to the requirement for a miniaturised propulsion system. The mass, power and volume constraints placed on this system by the host nanosatellite platform lead to the selection of a chemical propulsion system. In order to optimise the thrust available and minimise complexity a monopropellant system is a favourable solution. The research has considered the miniaturisation of two key components of a monopropellant thruster: the decomposition chamber and the nozzle. The focus was the extent of miniaturisation that was possible, while maintaining the use of a conventional approach in terms of manufacture and testing. Hydrogen peroxide was selected as the propellant due to its favourable handling characteristics and previous use at the Surrey Space Centre.

The geometry and morphology of a decomposition chamber are critical to the overall performance of the thruster. As the magnitude of thrust generated by the thruster reduces, the mass flow rate of propellant reduces together with the associated dimensions of the complete system. Empirical guidelines exist for the design of a decomposition chamber for a thruster of conventional size, however it is uncertain as to whether these remain applicable at thrust levels below 1 N. Two different catalyst morphologies were considered in decomposition chambers of various diameter and length. A manganese oxide catalyst, supported on a high density alumina foam was used to assess the performance of a monolithic catalyst bed and a silver powder was used to investigate the performance of a compressed powder catalyst bed. Catalyst deposition problems prevented a detailed assessment of the monolithic catalyst bed performance, but initial indications suggested that a ceramic foam of density greater than 20% was required. The tests with the compressed silver powder catalyst bed revealed that a decomposition chamber of 6.7 mm diameter and 5 mm length could successfully decompose hydrogen peroxide flowing at a rate of 0.6 gs^{-1} . In addition it demonstrated good cold-start characteristics with full decomposition evident in ambient conditions of 0°C with an initial propellant temperature of 4°C .

The thermal characteristics of a thruster are central to the resultant performance. The low mass flow rates of propellant used in a microthruster will result in less energy being released, therefore containment of the energy is critical. The high surface area to volume ratio of a microthruster

exacerbates the thermal losses, reducing the overall performance. The extent of this effect was investigated using a series of numerical models, designed to represent a decomposition chamber. The wall thickness of the chamber was varied to investigate whether an increase would reduce thermal loss. In fact the modelling has demonstrated that any additional mass increases the thermal losses. The material to be used in the construction must have high structural integrity but be able to withstand the extreme temperature range to which it will be subjected and be capable of being machined accurately. Three different materials were investigated, stainless steel 316, Macor[®] and silicon. Macor[®] was considered as it has a low thermal conductivity, allowing it to act as an insulating material. However, the modelling demonstrated that under steady-state conditions the low thermal conductivity of this material together with a high specific heat capacity combined to create a structure that contained heat within its bulk rather than insulating the chamber. Interest in the capabilities of MEMS manufacturing techniques led to the consideration of silicon as a structural material. The high thermal conductivity and specific heat capacity of this material mean that the structure quickly absorbs heat, but takes a long time to reach thermal equilibrium. Thus it was concluded that the chamber should be machined from a material such as stainless steel for ease of manufacture and strength, but a heat shield should be included in the design to reflect radiated heat back into the thruster.

The exhaust nozzle of a rocket thruster is designed to expand and accelerate the hot exhaust gases from the decomposition/combustion chamber. The efficiency with which this occurs is a function of the pressure and cross-sectional areas at the throat and exit of the nozzle. The flow of a fluid past a solid surface will result in the development of a boundary layer. The presence of a boundary layer within the nozzle will reduce the performance of a nozzle as it will reduce the throat and exit areas. To investigate the development of a boundary layer within an exhaust nozzle numerical models were created and solved using Fluent[®]. The results revealed that as the dimensions of the nozzle reduce, corresponding to reducing thrust levels, the thickness of the boundary layer at a given location increases. The effect of geometry on this result was assessed through the development of three additional series of models that each considered one aspect of geometry. One considered the divergence angle, one the throat contour and one the presence of the expanding section of the nozzle. The results from these models showed that increasing the divergence angle of the nozzle caused a further reduction in the performance observed, except in the largest case considered, corresponding to 500 mN thrust. Replacing the smooth throat contour with a sharp corner improved the performance, with the greatest improvement observed in the smallest case considered, corresponding to 1 mN thrust. Removing the divergent section of the nozzle completely reduced the performance significantly. This confirms that while the predicted performance of the nozzle is significantly reduced, a divergent section remains of value.

Contents

Executive Summary	i
Contents	iii
1 Introduction.....	4
1.1 Motivation for Research.....	4
1.2 Aims.....	4
2 Propellant Decomposition.....	2
2.1 The Chemistry of Catalysis.....	2
2.2 Performance Characterisation	4
2.3 Recommendations for Catalyst Pack Design	4
2.4 Assessment of Recommendations.....	6
2.5 Development of a Monolithic Catalyst Bed.....	7
2.6 Development of a Compressed Powder Catalyst Bed.....	14
2.7 Testing Set-up	18
2.8 Results & Discussion	21
3 Heat Transfer	33
3.1 Prediction of Thermal Losses	33
3.2 Conclusions.....	38
4 Nozzle Flow	38
4.1 Isentropic Nozzle Theory.....	39
4.2 Nozzle Inefficiencies.....	41
4.3 Development of Numerical Models.....	44
4.4 Solution Methodology	48
4.5 Presentation of Results.....	50
4.6 Results and Discussion	53
4.7 Conclusions.....	59
5 Conclusions.....	60
6 Recommendations for Future Work.....	61
7 Bibliography	62

1 Introduction

This report summarises the work completed under EOARD contract 043022 “Micro-Chemical Monopropellant Thruster”. The research was carried out at the Surrey Space Centre, University of Surrey and the testing was conducted at the Surrey Satellite Technology Ltd Propulsion Test Site, Westcott, Bucks.

1.1 Motivation for Research

The physics that govern the operation of a chemical rocket thruster is well understood at a conventional scale. Due to mass and power constraints there is increasing interest in the functionality of a chemical propulsion system to be capable of producing low magnitude thrusts. To achieve this goal successful miniaturisation of a complete propulsion system is required. Previous research studies have shown that the miniaturisation of a chemical propulsion system is a highly complex process. At micro scales, where characteristic dimensions are of the order of millimetres or less, it is critical that the physics of operation and the factors affecting them is clearly understood to ensure successful and efficient operation of the thruster. This research sought to explain some of the irregularities observed. A monopropellant system was selected to minimise complexity and the propellant used was hydrogen peroxide. For simplicity, it was proposed that the propulsion system should be considered in sections. This research focused on the decomposition chamber and nozzle components.

1.2 Aims

The research was characterised by three objectives, which are briefly outlined below:

- **Propellant Decomposition** – the optimum geometry and morphology of the catalyst bed
- **Heat Transfer** – the thermal characteristics of the decomposition chamber and nozzle assembly
- **Nozzle Flow** – the flow characteristics within the nozzle section of the thruster

2 Propellant Decomposition

This chapter is concerned with the efficient decomposition of the chosen propellant, hydrogen peroxide. The particular aspects of chemistry relating to the catalysis of the reaction is discussed first followed by a review of the available literature relating to the design of a catalyst bed for a hydrogen peroxide thruster. The two catalyst beds developed during the course of this research are then introduced and discussed together with the experimental results obtained.

2.1 The Chemistry of Catalysis

A catalyst is defined as a substance that accelerates a chemical reaction without being consumed in the process. The conversion of one substance into another requires chemical bonds to be both broken and created. Breaking bonds requires energy and making bonds releases energy. Initiation of a reaction, requires an activation energy, E_A , to break the first bonds. Introduction of a catalyst into a reaction allows this activation energy to be reduced, thereby accelerating the reaction. Figure 1 illustrates this, where the green path represents the catalysed pathway requiring a reduced activation energy to initiate the reaction.

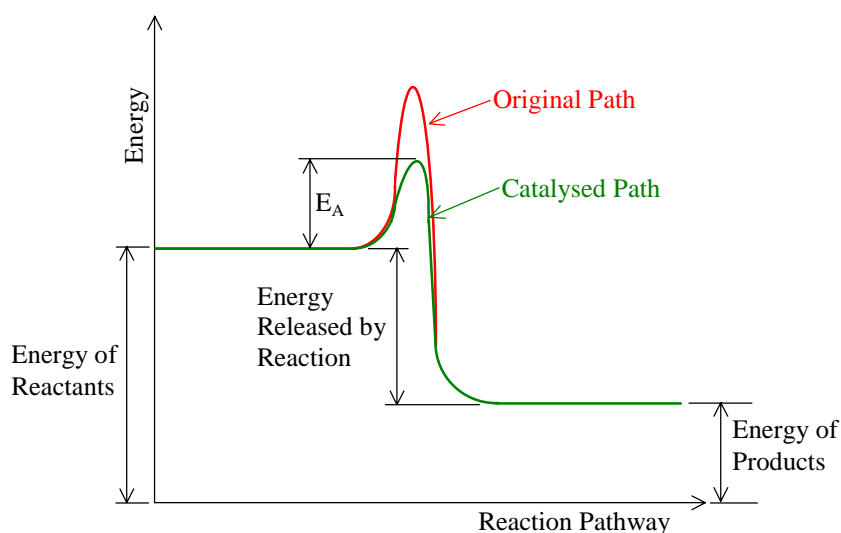


Figure 1: The Reaction Pathway

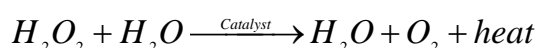
The reaction illustrated is an exothermic reaction, where the energy of the products is lower than that of the reactants, with the difference in energy being released as heat. In the case of an endothermic reaction the energy of the products is higher than that of the reactants and heat is absorbed.

Catalysis may be homogeneous or heterogeneous, dependent upon the phase of the catalyst compound in relation to the reactants [Atkins'97]. Homogeneous catalysis is when both the reactants and catalyst are in the same phase. Heterogeneous catalysis is when the reactants and catalyst are in different phases. In heterogeneous catalysis the catalyst is usually solid and the reactants either gaseous or liquid. The key advantage of using heterogeneous catalysis is that it is easier to contain, and therefore recycle, the catalyst material. The process of heterogeneous catalysis involves the reactants adsorbing onto the surface of the catalyst. This weakens the bonds within the reactants allowing the reaction to progress with a lower activation energy. Following the reaction the products are then desorbed from the surface and exhausted. The reaction takes place on the surface of the catalyst therefore it is pertinent to optimise the available surface area. For this reason a solid catalyst is usually in the form of a fine powder or a section of highly porous foam.

2.1.1 Catalysis of Hydrogen Peroxide

Hydrogen peroxide (H_2O_2) is very similar compound to water (H_2O) and it possesses similar physical properties. It occurs naturally and is found in low concentrations in streams and rivers, although it is an unstable compound and readily decomposes into water and oxygen. The decomposition reaction is exothermic and the temperature of the decomposition products is dependent upon the initial concentration of the hydrogen peroxide and the efficiency of the decomposition [McCormick'67].

The decomposition reaction of hydrogen peroxide may consist of up to twenty intermediate steps. Equation 1 represents the global reaction, and illustrates that the exhaust products are water and oxygen.



Equation 1: Decomposition of Hydrogen Peroxide

There are many known catalysts for the decomposition of hydrogen peroxide. In chemistry classes low concentrations of hydrogen peroxide may be catalysed using a small piece of liver or potato. At high concentrations a catalyst with a longer lifetime is required and interest moves primarily to silver and manganese oxides. Overall silver, in the form of compressed gauzes, is the preferred catalyst for the decomposition of hydrogen peroxide in a conventional thruster. The gauzes themselves are easy to handle thereby facilitating installation and compression within the chamber. The primary alternative is to use a manganese oxide catalyst, which will produce a faster reaction than silver, enabling a rapid start up characteristic [Kappenstein'05, Eloirdi'01]. It may be used as either a solution or a solid catalyst supported on another surface. Use of this catalyst in solution form requires the design of injectors to spray the catalyst onto the propellant,

which adds complexity to the system. It is difficult to create solid manganese oxide in any form other than a fine powder. For use as a catalyst it is therefore supported on a substrate, which provides the required structural strength.

2.2 Performance Characterisation

In order to compare the performance of a monopropellant thruster using different catalysts a characterisation parameter is needed. This should be a characteristic that is independent of the conditions downstream of the decomposition chamber. The characteristic used is the effective exhaust velocity, c^* , which is defined in Equation 2 as a function of the stagnation pressure in the decomposition chamber, p_c , the throat area, A^* and the mass flow rate of propellant, \dot{m} .

$$c^* \equiv \frac{p_c A^*}{\dot{m}}$$

Equation 2: Definition of the Effective Exhaust Velocity

This definition is a function of parameters that may be measured through experiment. Alternatively a definition of c^* that is based upon the propellant characteristics may be derived [Hill'92]. This is given in Equation 3, where γ is the ratio of specific heats of the propellant, \bar{R} is the universal gas constant, T_c is the temperature in the decomposition chamber and \mathcal{M} is the propellant molecular mass.

$$c^* = \sqrt{\frac{1}{\gamma} \left(\frac{\gamma + 1}{2} \right)^{\frac{\gamma + 1}{\gamma - 1}} \frac{\bar{R} T_c}{\mathcal{M}}}$$

Equation 3: Alternative Definition of the Effective Exhaust Velocity

Both of the definitions given for c^* demonstrate that it is a function of the propellant composition and the conditions within the decomposition chamber only. This makes it a suitable parameter for evaluating the efficiency of the catalyst.

2.3 Recommendations for Catalyst Pack Design

The size of the catalyst pack depends on various inputs, including the propellant concentration, operating pressure and allowable pressure drop. Standard operating conditions are assumed to be a chamber pressure of approximately 20 bar and temperature of 10 °C and above. An estimate of the required catalyst pack size may be made using empirical guidelines, however these assume that the catalyst is in the form of silver gauzes [Davis'60].

The first stage is to make an estimate of the mass flow rate required for a given thrust level, using Equation 4 [Davis'60]. Here \dot{m} is the mass flow rate of propellant, \mathcal{T} is the required thrust, I_{sp} the specific impulse of the propellant, η is the decomposition efficiency and g is the acceleration due to gravity.

$$\dot{m} = \frac{\mathcal{T}}{I_{sp} \eta g}$$

Equation 4: Mass Flow Rate Calculation

Based upon this equation, given that the ideal specific impulse of hydrogen peroxide is approximately 160 s, assuming an efficiency of 0.75 and a required thrust of 100 mN the mass flow rate is calculated to be $8.495 \times 10^{-5} \text{ kgs}^{-1}$.

The diameter of the catalyst pack is then calculated using Equation 5 [Davis'60], where A_c is the cross-sectional area of the pack and \mathcal{LF} is the loading factor.

$$A_c = \frac{\dot{m}}{\mathcal{LF}}$$

Equation 5: Cross-Sectional Area of the Catalyst Calculation

The literature suggests that for small diameter packs a loading factor of 59 – 117 should be used [Davis'60], although no indication is given of the bounding diameters to which this applies. Based upon the calculated propellant flow rate applying a \mathcal{LF} of 59 gives a pack diameter of 1.35 mm, while a \mathcal{LF} of 117 gives a pack diameter of 0.96 mm.

Finally the length of the catalyst pack is considered. From previous studies it is known that while the length of the catalyst bed has little effect on the start up characteristics, it has a direct influence on extent of decomposition observed for a given propellant flow rate [Willis'60]. For a given diameter of catalyst bed, a longer length will enable a higher flow rate of propellant to be completely decomposed. This implies that for a given mass flow rate there is an optimum catalyst bed length. A minimum length for the catalyst bed is suggested to be 31.75 mm to prevent incomplete decomposition, although the minimum diameter to which this relates is unknown [McCormick'67]. Other research has demonstrated that a catalyst pack length of 20 mm was optimal for a 12.7 mm chamber diameter, when filled with 100 compressed silver gauzes [Coxhill'02]. This suggests that the length of the catalyst bed should be investigated to determine the optimum size for a given diameter.

2.4 Assessment of Recommendations

The dimensions suggested by the design process outlined in section 2.3, result in a catalyst pack that is very long relative to its small diameter. There are several points that would require attention if a pack were to be developed based upon these figures, three of which will now be discussed.

2.4.1 Handling and Alignment Issues

The analysis above was based upon the assumption that silver gauzes were being used for the catalyst. For the thrust level of 100 mN considered the recommended diameter of the gauzes was 0.96 – 1.35 mm dependent upon loading factor. As discussed earlier in section 2.1.1, silver gauzes were the preferred solution for conventional hydrogen peroxide thrusters as they were easy to handle. In these cases the diameter of the gauzes is of the order of centimetres. Here, the significantly reduced diameter of the gauzes required, makes handling of them prohibitive. The gauge of wire and type of weave used for the gauzes would require careful selection to ensure structural integrity of the individual gauzes without excessive pressure drop once compressed. Finally the length of the catalyst required leads to potential alignment issues of the gauzes within the chamber.

2.4.2 Thermal Characteristics

The high surface area to volume ratio of a long thin decomposition chamber would exacerbate thermal losses. Hence the thermal characteristics are very unfavourable, as insulation of the chamber would be required to optimise the decomposition reaction. Instead a shorter catalyst pack with a larger diameter is preferable.

2.4.3 Physical Accommodation of Length

The reason for considering the miniaturisation of a monopropellant thruster was to enable a micro/nanosatellite to carry a propulsion system. Accommodating a chamber of the length specified would be impractical in this scenario.

Clearly the use of silver gauzes for a 100 mN hydrogen peroxide thruster is either not practical, or these design guidelines are no longer appropriate at this scale. This analysis in combination with the literature review reveals that the physical property appearing to dominate the efficiency of the reaction is the surface area of the catalyst available. To address this, two different avenues of research were pursued with respect to the catalyst structure: a monolithic catalyst bed, with the catalyst material supported on a high density ceramic foam and a compressed powder bed.

The overall aim of this research is to miniaturise the propulsion system to produce low magnitude thrust within a small system. Evaluation of the available literature has indicated that a reduced diameter catalyst pack will be required to accommodate the low mass flow rates associated with this objective. The aim of the remainder of this section is to develop an understanding of how the required geometry and morphology of the catalyst are modified as the magnitude of thrust decreases. To investigate the validity of the dimensions suggested by the empirical analysis, a larger catalyst pack diameter was selected for initial characterisation. The nominal diameter of the initial catalyst bed investigated was set to be 9.0 mm for both types of catalyst. Further reductions in the diameter of the silver catalyst bed were also achieved. The approaches used in each case together with the results obtained are outlined in the following sections.

2.5 Development of a Monolithic Catalyst Bed

Use of a monolithic catalyst bed allows scope for the catalyst material to be supported, therefore facilitating the use of a catalyst such as manganese oxides. This section will first evaluate the different monolithic supports available before summarising the steps taken to develop and test a monolithic catalyst bed based upon a manganese oxide compound.

2.5.1 Substrate Selection

A substrate for a monolithic catalyst should possess a number of qualities:

- High Specific Surface Area
- High Structural Integrity
- Low Pressure Drop

Each of these qualities is equally important. For example, if the specific surface area is high, but the structural integrity is low then the lifetime of the catalyst will be limited. In this scenario a lower specific surface area may be acceptable if this enables an increase in the structural integrity.

There are various media that may provide a useful solution. The supporting structure may be created in a method similar to that used to form a foam or artificially machined. Using MEMS manufacturing techniques it would be possible to develop an artificially porous structure. An example of this is shown in Figure 2, where the honeycomb structure on the left of the image is designed to form the substrate for a catalyst bed. The catalyst is deposited on the internal walls of each cell. The disadvantage of this approach is the bed length limitation of approximately 3 mm due to the issues relating to bonding wafers. The structure is strong and the pressure drop will be low, but the total specific surface area will also be low due to the short length. The Ångstrom

Space Technology Centre, Sweden developed these wafers as part of the collaborative work under European Space Agency contract no. 17091/03/NL/Sfe.

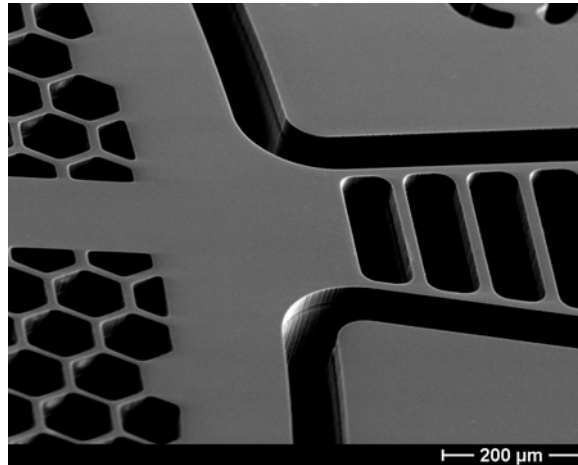


Figure 2: Etched Silicon Wafer ©ASTC

A similar approach applied to a different substrate material allows this length limit to be removed. Researchers at the University of Poitiers, are developing a catalyst bed based upon a mullite block, illustrated in Figure 3 [Kappenstein'05]. The block contains several 1 mm width channels, the inside wall of which are coated with catalyst. The geometry of the channels results in a low specific surface area. To improve this several layers of catalyst are deposited to create a rough surface and maximise the number of possible active sites for decomposition. The regular structure of the block leads to a high strength, but this also increases the possibility of viscous losses leading to a high pressure drop.

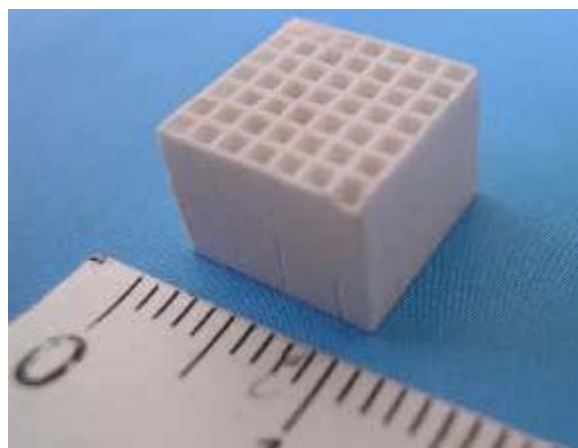


Figure 3: Mullite Monolith [Kappenstein'05]

A further option is to utilise a ceramic foam monolith. Various methods may be used to create a ceramic foam, with the most common creating a positive image of a host structure. A piece of polyurethane foam is saturated with a ceramic slurry, which is then solidified before the host structure is burnt away. The result is a reticulated structure that has large pores connected through

windows and separated by columns of ceramic [Richardson'00]. An example of a section of foam created using this method is shown in Figure 4, which illustrates significant variation in both pore sizes and the low structural density. The diameters of the pores in this image are in the range 0.04 – 1.5 mm.

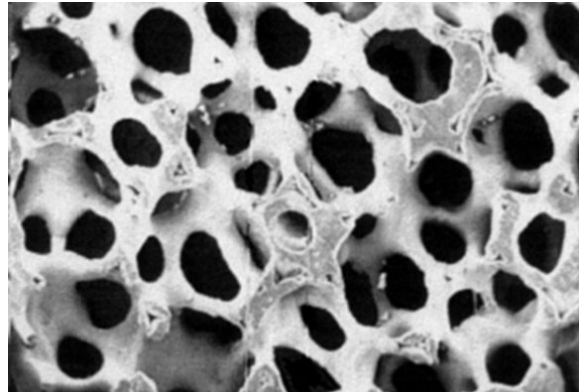


Figure 4: Reticulated Ceramic Foam [Richardson'00]

A foam manufactured in this way is suitable for applications where the stresses on the structure are low, for example in filters. The poor structural integrity of this type of foam makes it unsuitable for use as a catalyst substrate in the high pressure environment involved. In principle a ceramic is an ideal material for a catalyst substrate as it can withstand the high temperature and the oxidising environment better than most other materials. The success of a ceramic foam as a catalyst substrate is dependent upon the structural integrity of the material. The high pressure present within a decomposition chamber leads to the need for a high density foam for this application.

The percentage of solid material present within a section of foam i.e. the foam density, influences both the structural integrity and the specific surface area. It is the manufacturing process that limits the maximum foam density achieved. The Dytech Corporation Ltd uses an alternative production technique to that described above and foams with a significantly higher density result [Smith'04]. The density of the foam and average pore size can be selected during manufacture thereby allowing an optimal combination of properties for the desired application to be used. The manufacture of the foam is conducted in six stages:

i. Form a Dispersion

Ceramic powder is mixed with a liquid carrier and a polymerisable monomeric material.

ii. Agitate to Introduce Gas

A surfactant is added to the mixture, which is then agitated to create bubbles of gas.

iii. Allow to Polymerise

Once the required density is achieved an initiator is added to allow the monomer to polymerise within a mould.

iv. Dry

The foam is removed from the mould and dried slowly at first at room temperature before being force dried in an oven.

v. Shape

At this stage the ceramic is called “green” ceramic and it is easily machined into the desired shape.

vi. Fire in a furnace

The second drying phase in the furnace ensures the bubbles formed in the foam microstructure are solidified, resulting in the creation of a structure that contains pores with solid walls, instead of adjoining columns.

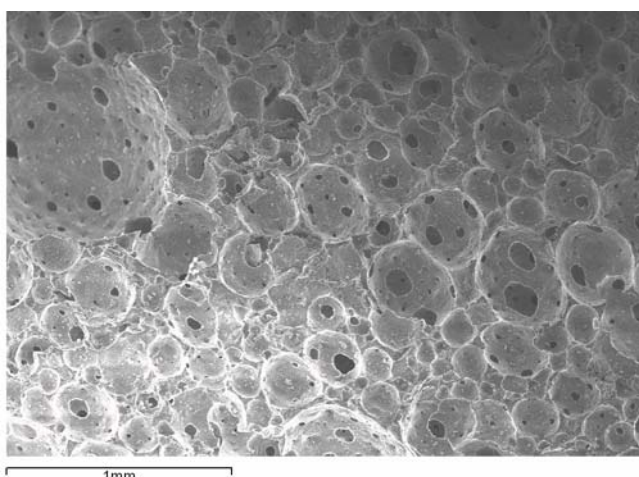


Figure 5: SEM Image of a 15% Density Foam

Windows within the pore walls cause the structure to be open-celled, while maintaining the superior strength and density. An example of the resulting high density structure of the foam is shown in the Scanning Electron Microscope image in Figure 5, where the foam density is 15% and the average pore diameter is 150 μm . The open cell nature of the foam is evident through the multitude of windows in the cell walls. The additional material present within this structure is immediately obvious in contrast to that shown in Figure 4. It is this added material in particular that increases the structural integrity of the material and raises the specific surface area.

This material was chosen as the substrate for the monolithic catalyst due to the favourable combination of properties it contains. Several different densities of this type of foam were considered as substrates for the catalyst to allow an assessment of the trade-off between structural

integrity and specific surface area. Figure 6 illustrates the visual differences in the range of foams used, where from left to right the foam densities are 10%, 15%, 20%, 23%, 27% respectively.



Figure 6: Range of Foam Density

2.5.2 Catalyst Selection and Preparation

The primary materials suitable for use as a catalyst for hydrogen peroxide in a monopropellant thruster were considered in section 2.1.1. It was found that silver and manganese oxides were the most suitable catalysts for this application. The low viscosity and high activity of a manganese oxide solution made it a favourable option for deposition within the porous substrate.

Various methods of preparation were investigated to ensure an even and thorough coating could be deposited throughout. The most successful method consisted of seven stages:

- i. Loose particulate was removed in an ultrasonic bath
- ii. The foam substrate was dried using a drying cabinet
- iii. A primary coat of potassium permanganate solution was deposited

Deposition of the catalyst on the foam was achieved by suspending one end of the foam cylinder and submerging in a saturated potassium permanganate solution. Capillary action drew the solution into the pores. The speed of this process is illustrated in Figure 7, where the time is in seconds. In this case a section of 20% density foam, 9 mm in diameter and 30 mm in length is being coated. For lower density foams the rate of deposition increases.

- iv. The foam was dried in a controlled environment at 4 °C
- v. A second coat of potassium permanganate was deposited
- vi. The foam was again dried in a controlled environment at 4 °C
- vii. The foam was placed into a furnace and heater to 900 °C at a rate of 3 °C per minute

Heating to 900 °C is necessary to decompose the water-soluble potassium permanganate solution into in-soluble manganese oxides and soluble potassium deposits, which were then removed

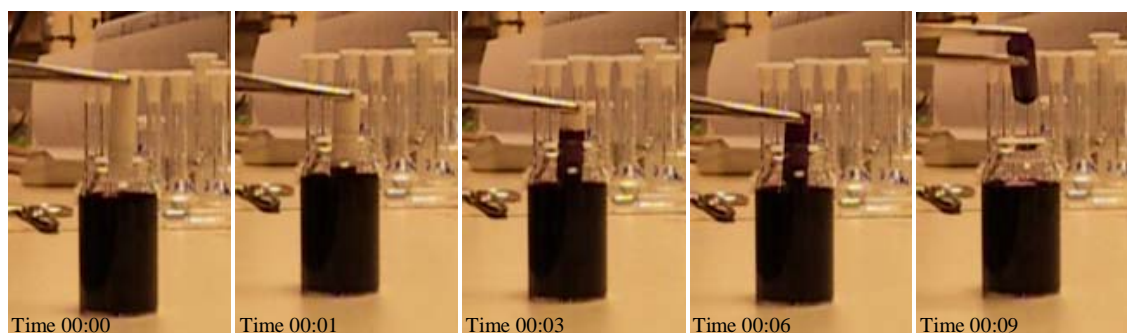


Figure 7: Saturation of an Alumina Foam with Potassium Permanganate Solution

The critical stage of the process was found to be step four, drying the catalyst onto the surface of the substrate. The rate at which the catalyst material dried was found to significantly affect the quality of catalyst deposition. Figure 8 shows two different ceramic foams of the same density that were dried in different conditions. The foam in the left image was dried at room temperature, while the foam in the right image was dried in a temperature controlled environment at 4 °C.

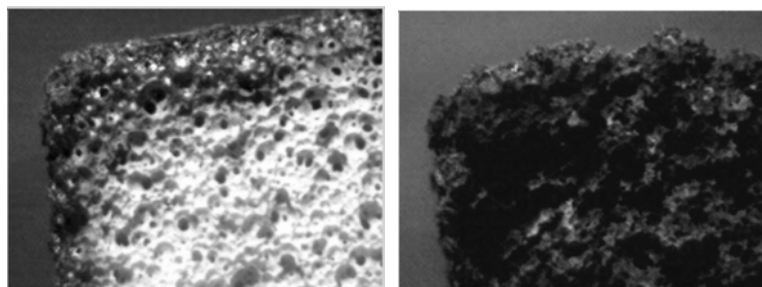


Figure 8: Comparison of Manganese Oxide Deposition at 100x Magnification

The images were taken using an optical microscope combined with a digital camera eyepiece. The thin dark band around the edges of the foam in the left hand image is coupled with a very light central region, indicating that most of the catalyst has deposited at the edge of the foam with almost none remaining in the interior. Little variation in colour is observed in the right hand image, indicating an even covering of catalyst. It is thought that the catalyst solution was drawn back towards the surface of the foam during the drying process at room temperature as a result of capillary forces. Drying at the colder temperature where the solution remains more viscous throughout the drying phase appears to eliminate this effect. A sample of the manganese oxide deposit was analysed using X-Ray Diffraction and the results indicate that the compound was predominantly Mn_3O_4 .

An alternative deposition method that was tried utilised flash vaporisation to dry the catalyst faster than it could draw out. This appeared to achieve reasonable results, however the deposition remained uneven throughout the catalyst as shown by Figure 9, where the two ends of the block exhibit a significantly lighter colour indicating a lack of catalyst material. The squares are 5 mm across for scale.



Figure 9: Flash Vaporisation Deposition

Initially three different densities of foam (10%, 15%, 20%) were prepared for testing using the first deposition method described. Following initial tests higher density foams were also prepared due to structural issues.

2.5.3 Catalyst Testing Preparation

The next phase was to prepare the catalyst coated cylinders for testing with hydrogen peroxide by securing them within a suitable chamber, formed of a section of stainless steel tube. A layer of magnesium oxide based ceramic adhesive (Aremco Ceramabond™ 571) was deposited onto the surface of the foam, to ensure that the exterior pores were sealed. Before the adhesive dried completely it was moulded using a pre-cut section of steel tube to ensure it would fit into the required section of tube. The adhesive coated foam was then left to air-dry for an hour before it was placed in the furnace at 93 °C for two hours to cure. The second stage was to bond the sealed foam into a sleeve using the additional ceramic adhesive. Figure 10 shows an axial cross-section of a finished test section.



Figure 10: Section of Catalyst Bonded into Sleeve

It was essential that the bond between the sleeve and the catalyst was sufficient to prevent any propellant from escaping the catalyst and to prevent the catalyst from moving within the casing. Before the test pieces were exposed to hydrogen peroxide, pressure drop tests were performed on each piece to evaluate the bond. The mass flow rate of nitrogen, at a given pressure, through each of the test pieces was monitored to determine the quality of the bond. The objective of this was to establish that the bond was sufficient by a good correlation of results between different samples for a given density. This also ensured that any test pieces with poor bonds between the foam and the sleeve were quickly identified, as a result of the unusually low pressure drops observed. An

example of the testing data for 20% density foam is shown in Figure 11. It is clear that three test pieces have bonded successfully and one has not, which results in the higher mass flow rate. The error bars placed on to the plot account for the errors associated with the mass flow rate and pressure data, 5% error for the pressure transducer and 2% for the mass measurement.

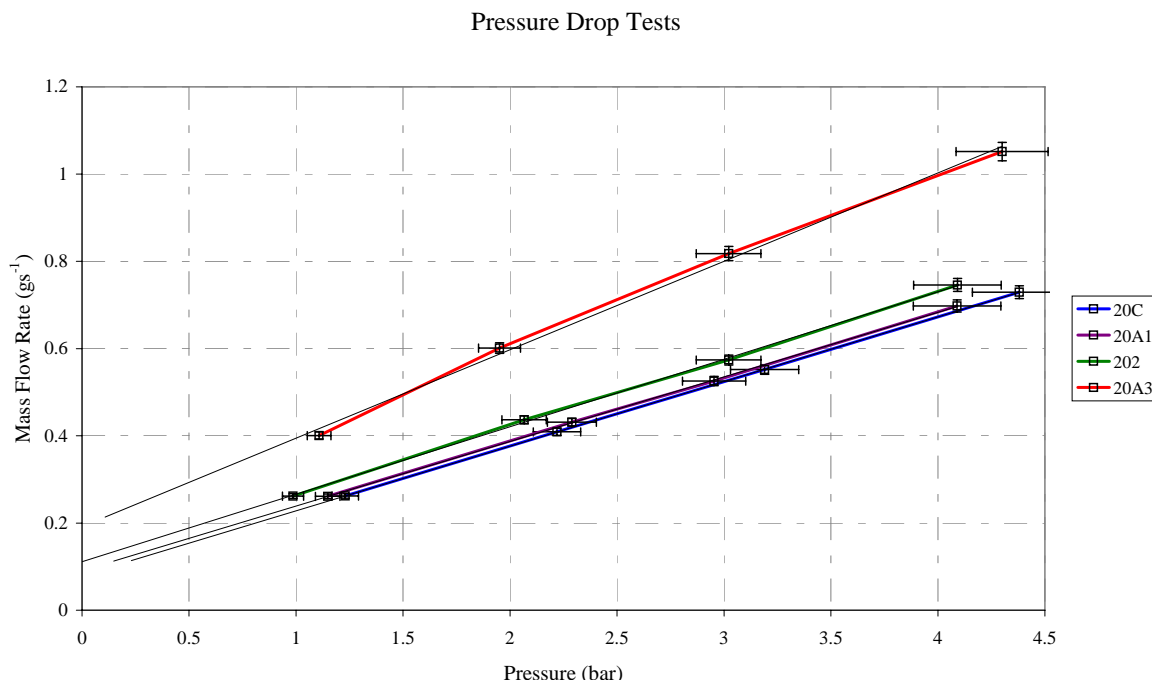


Figure 11: Pressure Drop Test Data for 20% Density Foam

A linear trendline was created for each data series and it fell within the error bars in all cases. All of the test pieces that passed the pressure drop test were then ready to be tested with hydrogen peroxide.

2.6 Development of a Compressed Powder Catalyst Bed

The key aspect of the monolithic catalyst bed development was the deposition of the catalyst material onto the substrate. In contrast the key aspect of the compressed powder catalyst bed development was the design of a chamber suitable to hold the correct volume of catalyst. This section will first discuss the different materials that were available for use as the catalyst then outline the design used to test the performance of the catalyst.

2.6.1 Catalyst Material Selection

The catalyst used for the monolithic bed was a supported material allowing use of manganese oxides, which are difficult to generate as an unsupported solid. For a compressed powder bed the option of using ceramic beads to support a catalyst was available but the literature revealed only limited success with this approach [Eloirdi'01]. The alternative was to use a powder, where the

size of the particles was selected such that the surface area was sufficient to maintain decomposition without the pressure drop becoming prohibitive. It was decided that the most practical method of achieving this was to use a powder of solid silver. The size of the particles used was selected based upon the pore size of the ceramic foam used previously. Two different grades of powder were selected, one coarser than the other to enable an investigation as to the influence of surface area and pressure drop at this scale. The coarser powder had a particle size range of 680 to 1600 μm , while the finer powder had a particle size between 150 and 200 μm .

2.6.2 Design of a Catalyst Test Chamber

The key consideration in the design of the chamber to contain the silver powder was the flow path of the propellant. It was essential that the propellant would be forced through the catalyst itself and not bypass around it. To achieve this the powder should be under compression thereby presenting a fixed impediment for the propellant to negotiate.

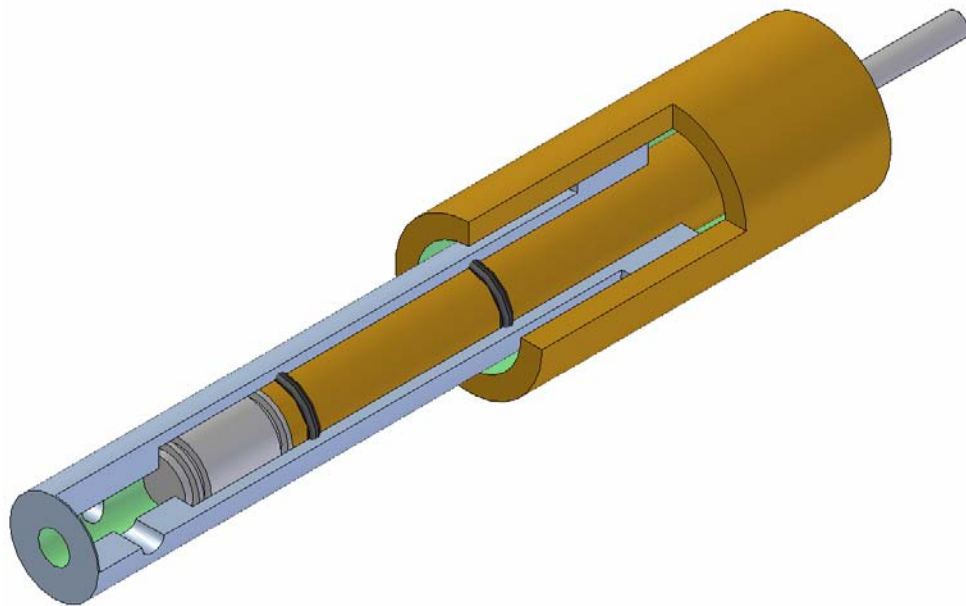


Figure 12: CAD Model of Powder Test Chamber

Figure 12 shows a sketch of the final configuration of the design. It consists of three key sections, the chamber itself, a plunger section and a compression device. The chamber has a nominal internal diameter of 9.7 mm, which is comparable with the diameter of the monolithic catalysts used. The plunger section accommodates two o-rings, 7 mm internal diameter and 1 mm cross-section. These create a seal between it and the chamber wall.

The length of the various components was set to allow a variation in the catalyst pack length from 0 – 40 mm to be investigated. This placed some constraints on the materials that were suitable for the manufacture of the chamber due to the depth of the bores required. Two holes were drilled in

the wall of the chamber downstream of the catalyst. This allowed a short section of tube to be located in each, enabling a pressure and temperature measurement to be taken. At the end of the chamber a hole was created and threaded with an M5 fine thread. The throat was created using a brass insert, which was screwed into the thread created. This facilitated the unloading of the catalyst after firing.

A pleated stainless steel filter disc, manufactured by Microfiltrex was located either end of the catalyst material to contain it and enable compression. The mesh size chosen for the filter was 60 μm to ensure no loss of powder with minimal pressure drop.

To reduce the diameter of the catalyst within the chamber a series of collars was created to fit inside the chamber. Two different sets of collars were used to create two additional chambers. The wall thickness of the first collars was 1 mm, causing a reduction in diameter of 2 mm to 7.7 mm. The wall thickness of the second collars was 1.5 mm, causing a reduction in diameter to 6.7 mm. The filter discs were located either end of the collar to maintain the flow path through the catalyst.

2.6.3 Catalyst Testing Preparation

The pressure drop through a 9.7 mm diameter catalyst pack was evaluated for a given length of powder using a set up similar to that described previously for the monolithic chamber. The silver powder was weighed into discrete amounts to enable evaluation of the resultant pack length and density.

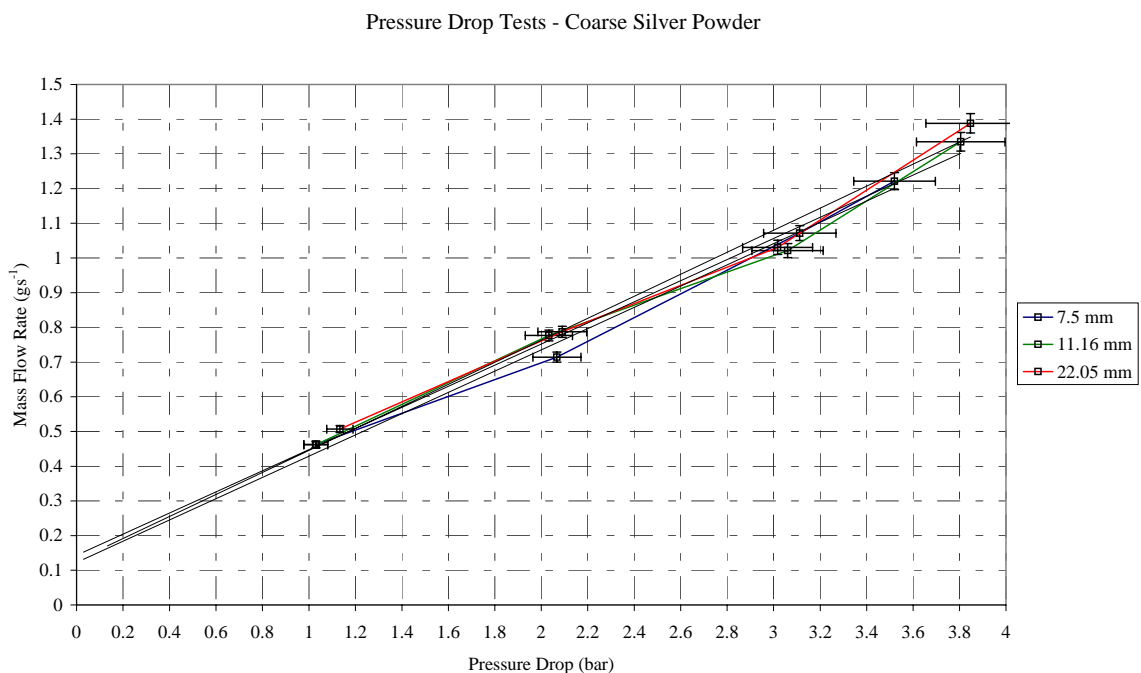


Figure 13: Pressure Drop Test Data for the Coarse Powder

The two different grades of powder used corresponded to two different pack densities. Different lengths of pack were then investigated to determine the change in the pressure drop observed. The results from the tests are shown in Figure 13 and Figure 14.

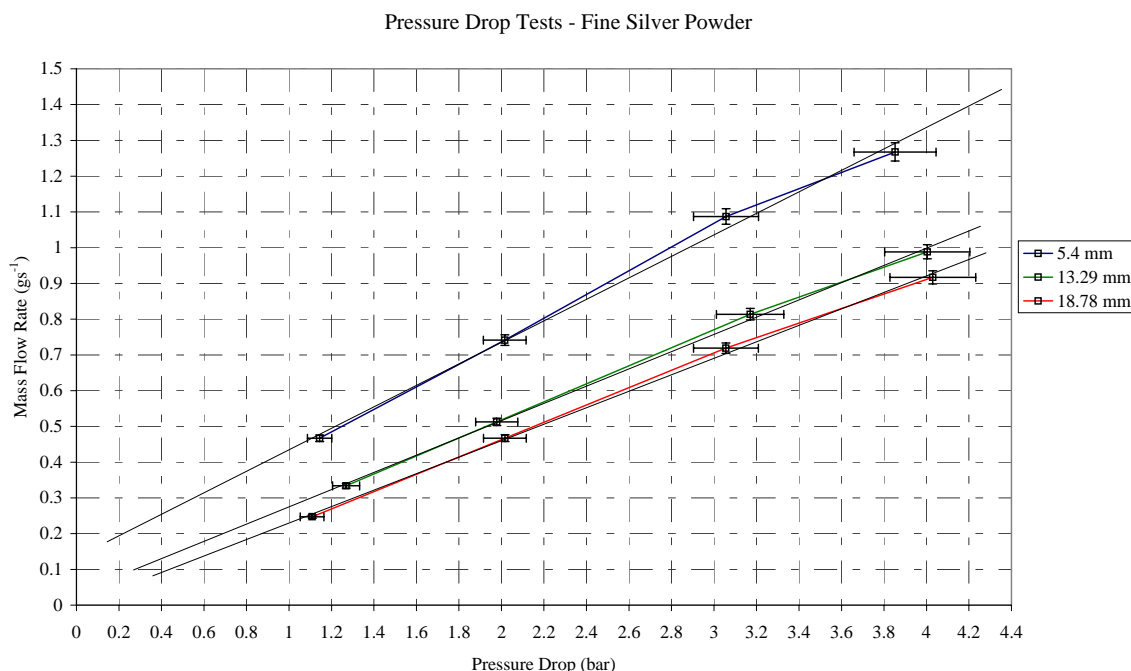


Figure 14: Pressure Drop Test Data for the Fine Powder

The lengths of the catalyst beds that resulted from the masses of powder selected varied, as the packing density assumed initially was too high. The shape of the powder grains prevented a close packing density, hence the lengths of catalyst bed that resulted were longer than predicted.

Prior to testing the length of each catalyst pack was measured using Vernier Calipers to validate the estimated packing density. The shorter lengths of the fine powder packs indicated a higher packing density and increasing the pack length of the fine powder resulted in an increase in the pressure drop as expected.

There is little difference in the data collected for the coarse powder for the different lengths of pack investigated. This indicates that the pressure drop through the pack is very low and is consistent with the voids between the powder particles being relatively large.

This data allowed the approximate packing density of each silver powder to be calculated. For the coarse powder this was estimated to be 0.41 and for the fine powder 0.47. From these figures the mass of powder required for use in each of the chambers was calculated. The data corresponding to the different lengths of catalyst tested in the 9.7 mm, 7.7 mm and 6.7 mm diameter chambers is given in Table 1, Table 2 and Table 3 respectively.

Length	Fine Powder	Coarse Powder
5.0 mm	1.825 g	1.590 g
7.5 mm	2.738 g	2.385 g
10.0 mm	3.650 g	3.180 g
12.5 mm	4.563 g	3.975 g

Table 1: Mass of Catalyst Required for a Given Length in the 9.7 mm Diameter Chamber

Length	Fine Powder	Coarse Powder
5.0 mm	1.140 g	0.995 g
7.5 mm	1.710 g	1.493 g
10.0 mm	2.280 g	1.990 g

Table 2: Mass of Catalyst Required for a Given Length in the 7.6 mm Diameter Chamber

Length	Fine Powder	Coarse Powder
5.0 mm	1.140 g	0.995 g
7.5 mm	1.710 g	1.493 g
10.0 mm	2.280 g	1.990 g

Table 3: Mass of Catalyst Required for a Given Length in the 6.7 mm Diameter Chamber

2.7 Testing Set-up

All testing with hydrogen peroxide was conducted at the SSTL propulsion test site at the Westcott Venture Park, Westcott, Bucks. The handling procedures outlined in the hydrogen peroxide handbook were followed at all times and full protective clothing was worn when in proximity to the propellant [Constantine'67].

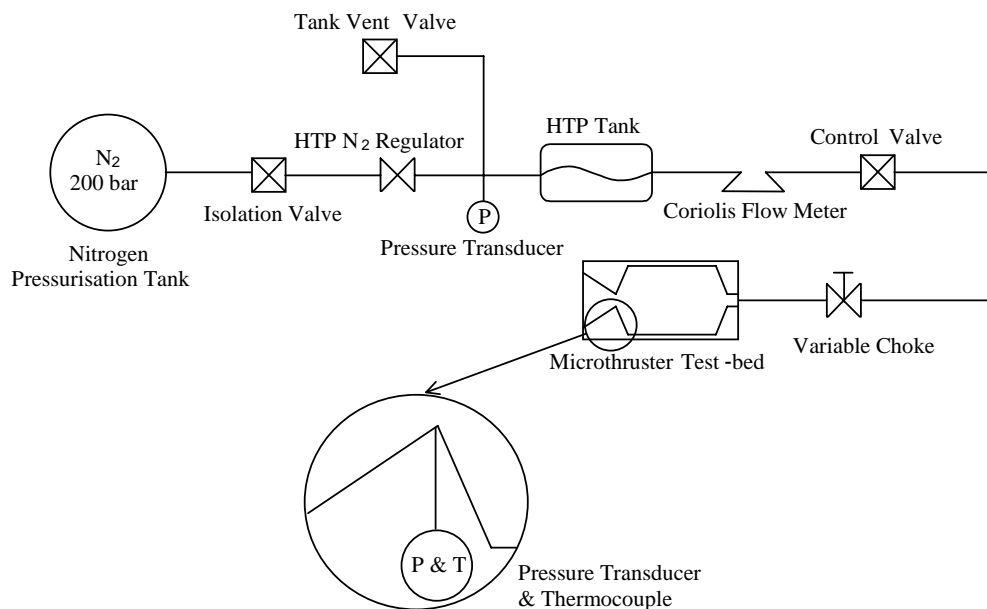


Figure 15: Schematic of Testing Set-up

The test-rig used to characterise the performance of both catalysts was based upon a set-up used in previous work [Coxhill'02]. It consisted of three sections; the propellant feed system, the

catalyst test bed and the data acquisition set up. A general schematic of the layout of the propellant feed system and catalyst test bed is shown in Figure 15. Not all instrumentation was present for the tests with the monolithic catalyst.

2.7.1 Monolithic Catalyst Test Set-up

The $\frac{1}{2}$ inch steel tubes containing the catalyst were attached to the $\frac{1}{4}$ inch propellant feed system pipes using standard Swagelok[®] reducing union fittings, as shown in Figure 16. This allowed the test piece to be changed easily, while maintaining a good seal. The image also shows the location of the thermocouple downstream of the catalyst and the 1mm diameter choke used.

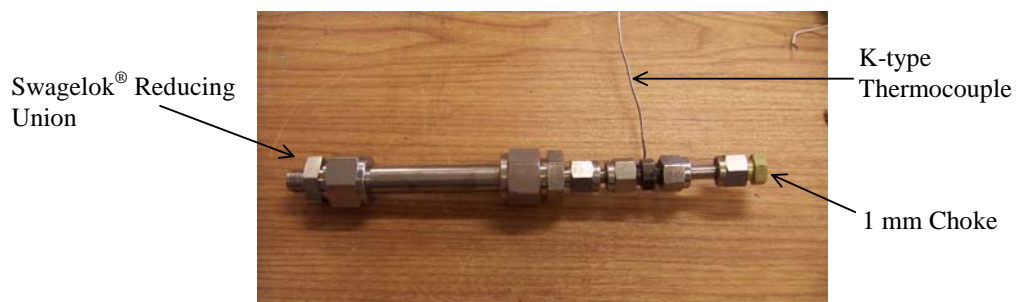


Figure 16: Monolithic Catalyst Test Piece

The performance of a monopropellant thruster may be characterised by the extent of decomposition achieved and the smoothness of the reaction. Initially a single temperature measurement was recorded then, as the behaviour of the catalyst became better understood, mass flow data was also recorded.

2.7.2 Compressed Powder Catalyst Test Set-up

The design of the test chamber used for the compressed powder catalyst tests was discussed in section 2.6.2 and is shown in Figure 17. This was connected to the propellant feed system through use of standard Swagelok[®] fittings. The two short sections of tube located in the side of the end section of the chamber were used to locate instrumentation. One contained a thermocouple and the other ended in a fitting allowing a pressure transducer to be located at the end of it. The fixed length of the tube between the pressure transducer and the flow allowed the small error in the data recorded to remain constant. The thermocouple was brazed into position with the tip located in the centre of the exhaust flow.

The catalyst was loaded into the chamber immediately prior to testing. A filter was inserted into the chamber first, followed by the silver powder. The second filter disc was carefully inserted to ensure it remained normal to the flow direction. The o-rings were moistened using a little

distilled water and the plunger section was inserted into the chamber. Finally the compression section was screwed into place.



Figure 17: Compressed Powder Test Set-up

2.7.3 Instrumentation

The instrumentation system used to record data was originally developed for previous work [Coxhill'02]. The output signals from the sensors used were converted from a current to a voltage via a data acquisition card (DAC), manufactured by National Instruments. Each signal was registered to a particular channel of the sixteen available. The current from the sensors was in the range 4 – 20 mA, which was converted to a voltage in the range 0.88 – 4.4 V through use of a 220 Ω resistor. This voltage was then fitted to the 0 – 5 V range of the card and detected by the analogue to digital converter (ADC) within the PC. The software used to monitor the card was the National Instruments LabVIEW[®] system and both the calibration and acquisition programs written for the previous research were used for this research.

The flow rate of the propellant was initially measured using a Micro Motion[®] model D coriolis flow meter, which utilises coriolis forces to measure the flow rate. The fluid passes through a vibrating pipe, generating coriolis forces, causing a phase shift in the sensor signals that are proportional to the flow rate. The key advantage of this technique was that the flow measurement is entirely independent of the pressure, viscosity, density and temperature of the fluid. The coriolis flow meter used was accurate to within 1% of the scale reading for a flow rate as low as approximately 0.8 gs^{-1} and to within 13% of the scale reading for a flow rate of approximately 0.4 gs^{-1} . As the propellant flow rate reduced below this a different set up was required to monitor the flow rate. A propellant tank was placed onto a set of digital scales that was linked directly to the computer. This logged the mass reading at a rate of 1 Hz. Plotting this data with respect to time

allowed the average mass flow rate to be calculated. When testing the set up a steady mass flow rate of 0.07 gs^{-1} was achieved.

The temperature of the exhaust products was measured using an insulated K-type thermocouple placed downstream of the catalyst. This type of thermocouple will operate up to a temperature of 1000°C , so was ideal for placement in the exhaust flow, where the maximum temperature of the decomposition products was predicted to be approximately 600°C . The output signal from the thermocouple was amplified using a temperature transmitter amplifier. These amplifiers are cold junction compensated and when a 24 V supply is supplied they output a signal in the range 4 – 20 mA. Calibration of the output current was achieved through use of a thermocouple simulator.

The static pressure was measured using standard pressure transducers, manufactured by RS Components Ltd[®]. The transducers contain strain gauges, which are bonded to a diaphragm. Application of pressure moves the diaphragm introducing a strain in the gauges. This was measured as an electrical resistance, the magnitude of which was proportional to the pressure present. The transducer used was calibrated in the propulsion laboratory on campus using the commercially calibrated pressure panel.

2.8 Results & Discussion

This section will review the results generated through the testing of both types of catalyst. The variations investigated and trends observed will be discussed.

2.8.1 Monolithic Catalyst Bed Results

Several samples of each density of catalyst were tested using the set up described above. The data recorded was repeatable and generated temperatures in excess of 500°C . The initial tests were conducted using the lower density foams, which have the highest internal surface area. An example of the temperature data recorded for the monolithic catalyst bed is shown in Figure 18, for a 15% density foam.

The initial temperature rise to 300°C took place in two stages with a small plateau appearing at approximately 175°C . This is thought to correspond to the boiling temperature of hydrogen peroxide and appears on all temperature traces when the initial temperature is below approximately 150°C . The temperature rise from 300°C to 500°C occurred at a significantly slower rate, which is thought to be due to the thermal characteristics of the set up as no insulation was present.

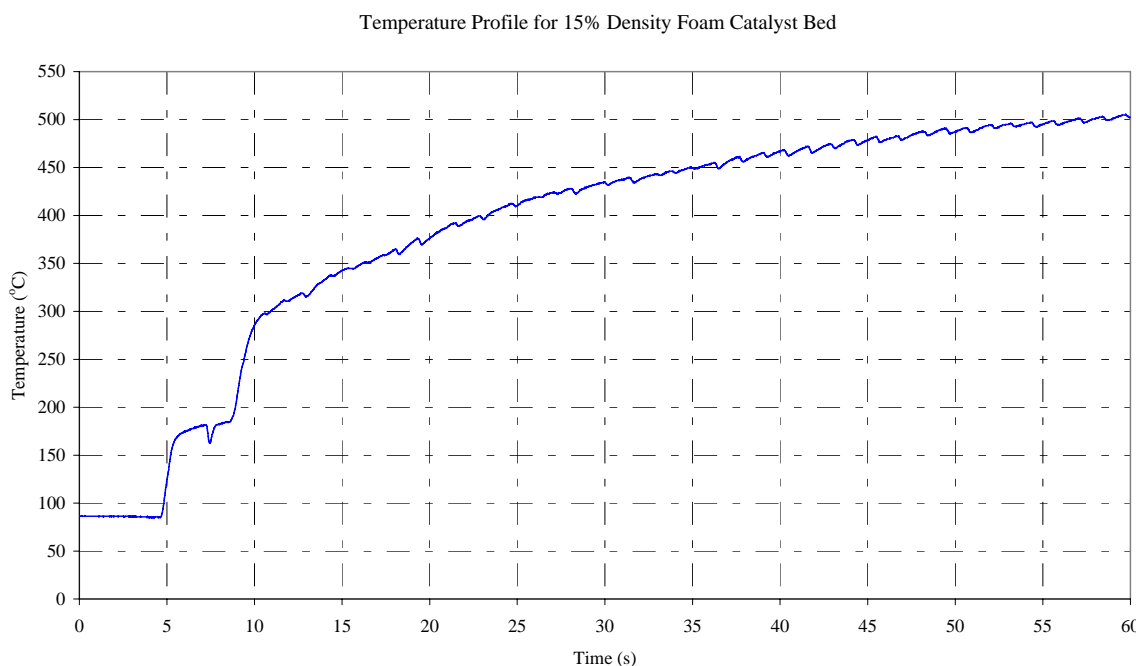


Figure 18: Temperature Profile for a 15% Density Foam

The shape of this temperature profile implies that the flow through the catalyst is not smooth. The rough shape of the profile indicates that the decomposition process accelerates and slows in quick succession. The inlet conditions to the catalyst were varied in an attempt to reduce the severity of these oscillations however little change was observed. The coriolis mass flow meter was added to the set up to provide additional information about the flow environment. Data was recorded for test runs with 20% density foam catalysts, an example of which is shown in Figure 19, where the temperature trace is shown in blue and the mass flow data in red. In general an initial peak in the mass flow rate data is expected as the void upstream of the catalyst is filled, following this peak the flow should become smooth. This is not the case for the data shown, where an oscillatory pattern is evident throughout indicating unsteady flow within the thruster.

Inspection of the data reveals a link between the time period of the oscillations in both traces. One cycle for the mass flow rate data includes a sharp peak followed by a flat section. The temperature data exhibits a saw-tooth profile but maintains a steady climb overall. There are many factors that may contribute to this instability, including the energetic nature of the decomposition reaction and the void immediately upstream of the catalyst. Previous work with hydrogen peroxide highlighted the need to minimise the void volume immediately upstream of the catalyst pack [McCormick'67]. The flat sections in the mass flow rate data correspond to reversed flow. The mass flow meter used can not register this, but movement of the flow pipes themselves indicated movement of the propellant. The shape of the temperature profile supports this interpretation, as the peaks in the mass flow rate corresponds to the troughs in the temperature profile. It appears that the high flow rate reduced the temperature, but filled the catalyst. When

the flow reversed the propellant left in the catalyst decomposed, causing the temperature to rise again. The frequency of these oscillations is high initially and reduces as the temperature of the exhaust products increases, however the exact reason for this remains unknown.

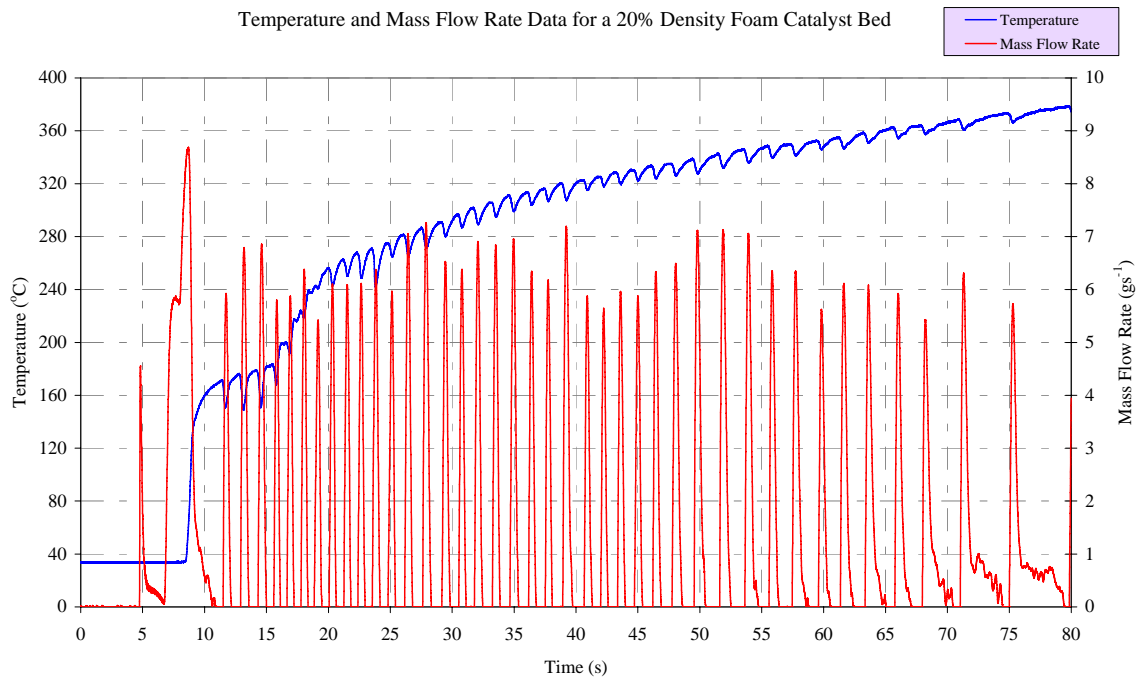


Figure 19: Temperature & Mass Flow Rate Data for a 20% Density Foam

The presence of these oscillations raised concerns about the useful lifetime of the ceramic foam as a catalyst. Following testing of the lower densities of foam a significant amount of powder was found to be loose at the upstream end of the catalyst.

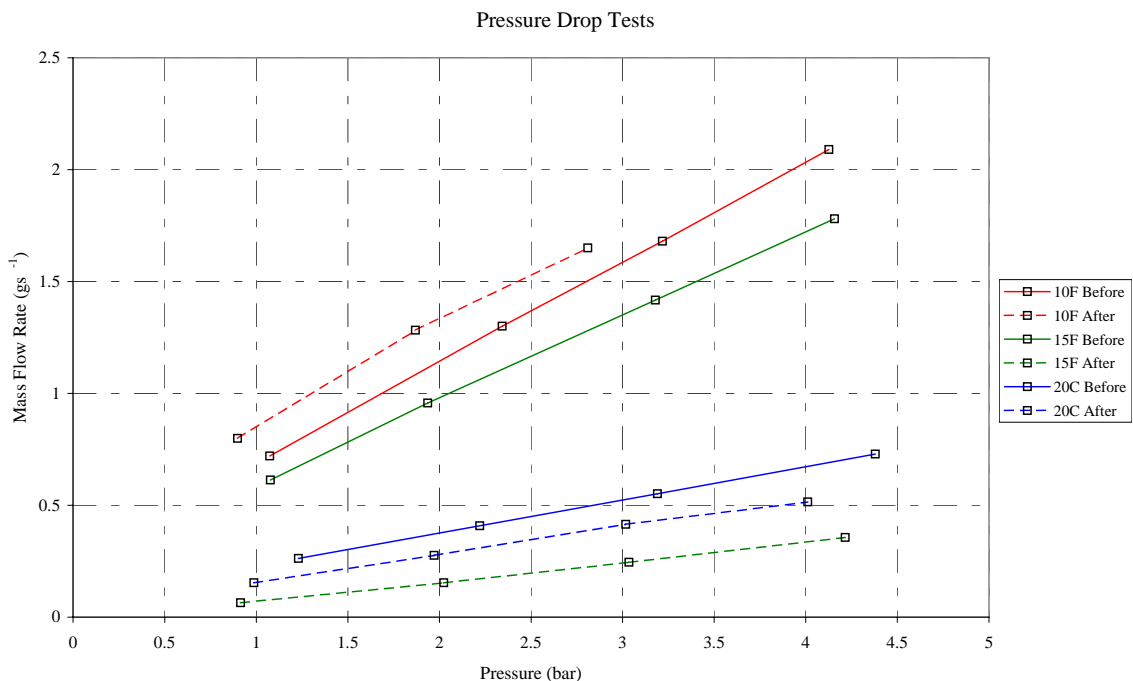


Figure 20: Pressure Drop Tests Following Firing

To evaluate the extent of the internal damage, pressure drop tests were conducted on the test pieces after firing. The effect of the firing on the internal structure of the catalyst itself was immediately evident and an example of the pressure drop data before and after testing for the lower density foams is shown in Figure 20, where 10F is a 10% density foam, 15F a 15% density and 20C a 20% density foam.

The firing clearly affected all of the foam catalysts although not in the same way. The pressure drop through the 10% density foam reduced, while for the other two foams shown it increased. It was decided that a visual inspection of the interior of the foam was required in order to investigate the reasons for these contrasting results. This was achieved by filling the catalyst with a low viscosity adhesive, Loctite[®] 420, which allowed them to be sectioned for visual inspection. To ensure the adhesive was present throughout the foam a soft vacuum was created at one end of the catalyst using a water pump. The three foams corresponding to the data above are shown in Figure 21, where the flow direction during testing was from left to right.

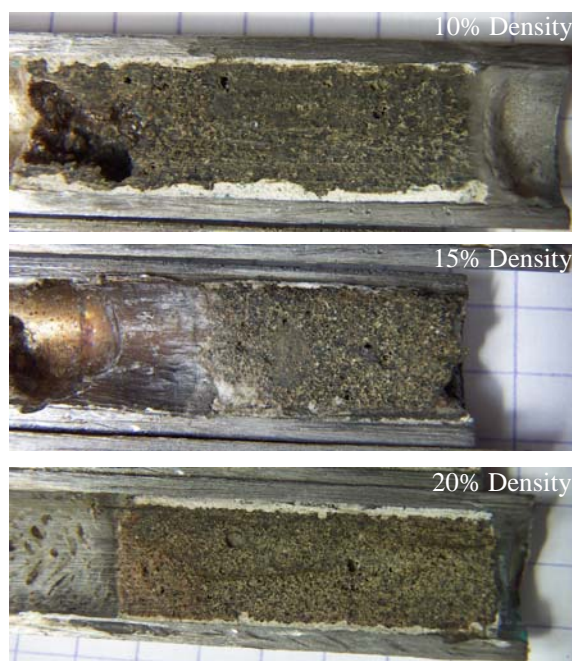


Figure 21: Filled Section Catalysts

The images reveal the extent of degradation that occurred within the foam itself. In the case of the 10% density foam, a significant cavity is present at the upstream end of the catalyst, indicating a very energetic reaction has taken place. The removal of material, combined with severe degradation of the remaining internal structure supports the reduced pressure drop observed for this catalyst. Inspection of the 15% density foam reveals that approximately 40% of the initial catalyst material has broken down. The total operation time for the 15% density foam was appreciably longer than that of the 10% density foam, leading to the greater degradation. However the pressure drop increased, not decreased as would have been expected if this

additional loss of material were the only explanation. In addition to the void, loose material can be observed at the upstream end of the foam. This material will cause the pressure drop to increase above the initial value as it artificially increases the density of the structure in this region. This theory is supported by Figure 22, which shows an enlarged section of the 20% density foam upstream of the catalyst. The 20% density case also exhibited an increased pressure drop after firing. In this image it is possible to identify substrate particles embedded within the adhesive. While these are no longer compressed at the upstream face of the catalyst, their presence supports the theory outlined above. In addition the smaller amount of material lost in the 20% density case corresponds with the lower increase in pressure drop observed.

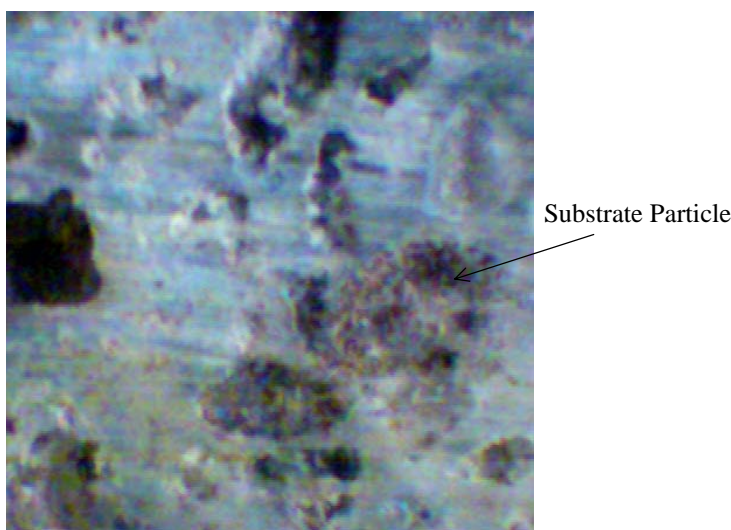


Figure 22: 20% Density Foam Post Firing

This inspection revealed the fragility of the low density foams. Catalysts based upon a higher density substrate (23%, 27%) were therefore created to investigate the impact of the stronger structure on the performance. The results from testing these foams were very encouraging with respect to the pressure oscillations previously observed, however the maximum temperature achieved was disappointing. An example of the data generated using the 23% and 27% density foams with respect to the 15% density foam shown before is given in Figure 23. The green trace corresponding to the 23% density foam is significantly smoother than that of the 15% density case, and indicates a considerably smoother decomposition characteristic.

Following the previous tests when good temperature characteristics were generated using the manganese oxide catalyst, the low performance was unexpected. It had been necessary to change the method of catalyst deposition at this time from the initial method described in section 2.5.2 to the flash vaporisation method. The chilled environment used to dry the catalyst onto the surface of the foam suffered a change that was undeterminable. The result of that change was to increase the drying rate, resulting in deposition similar to that observed when the catalyst dried at room temperature. As a result the flash vaporisation technique described in section 2.5.2 was developed

with outwardly good results. Following the test runs conducted, where low decomposition temperatures were observed the method of catalyst decomposition was considered as a source of the poor performance. Internal inspection of the catalysts led to the discovery of the uneven deposition that was shown in Figure 9. The lower catalyst loading is believed to cause the reduction in temperature achieved. The improved decomposition characteristic demonstrates that the increased pressure drop associated with the higher density foam is favourable.

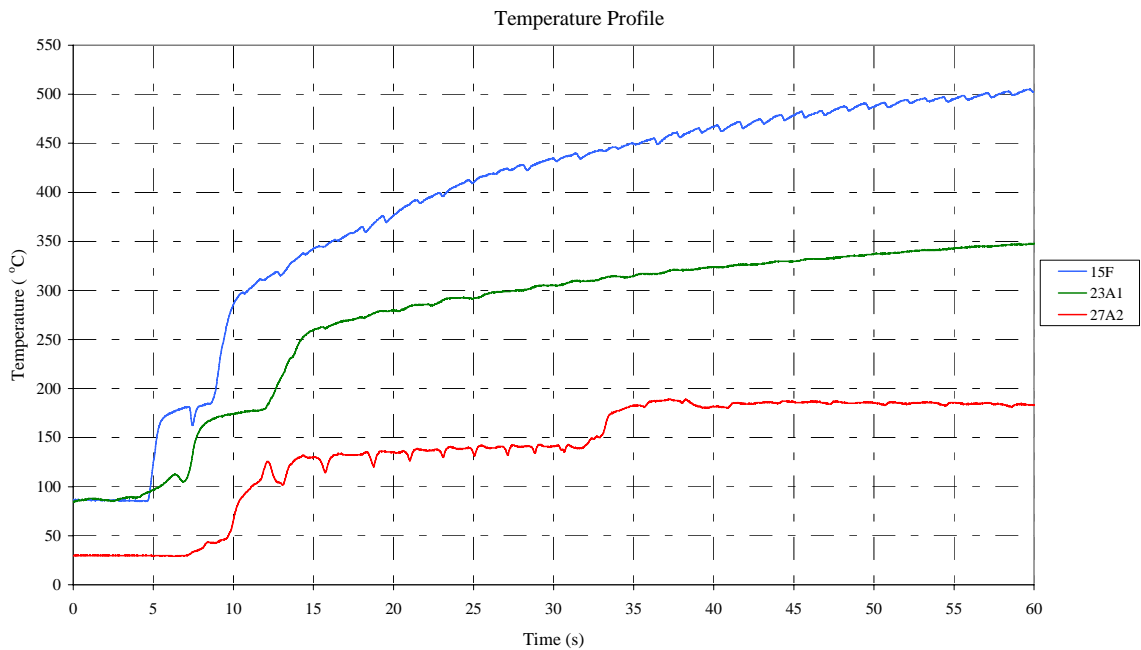


Figure 23: Temperature Profiles for Higher Density Foams

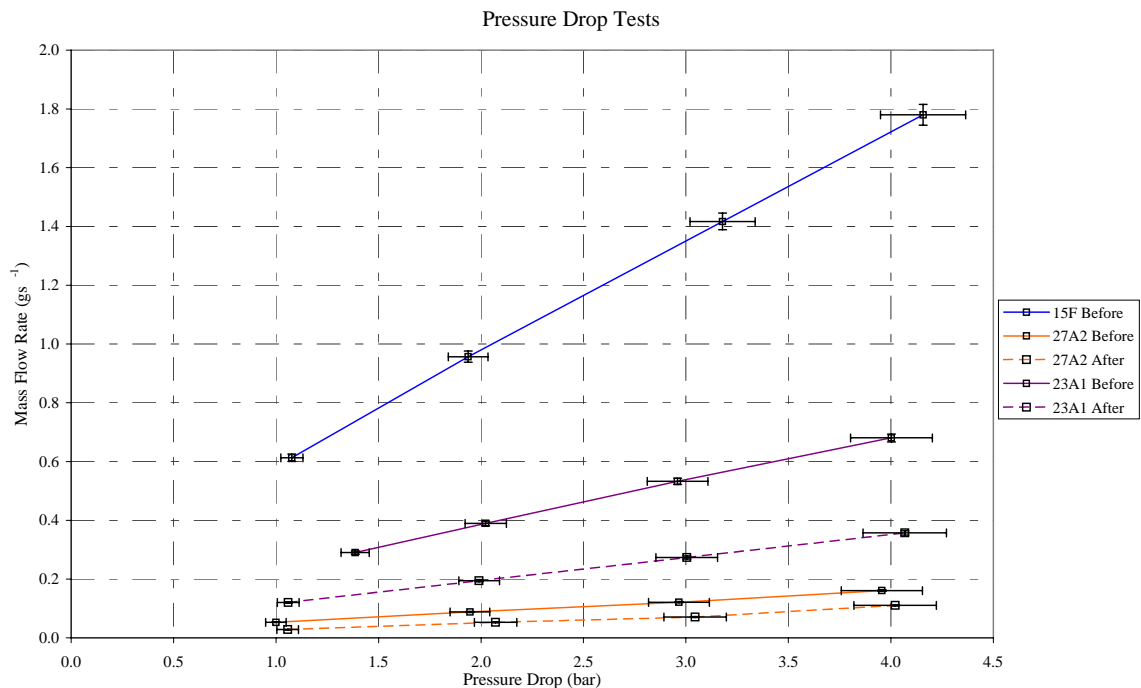


Figure 24: Higher Density Foams Pressure Drop Tests Following Firing

To investigate this further pressure drop tests were again conducted on the catalysts after firing.

To investigate this further pressure drop tests were again conducted on the catalysts after firing. The total firing duration will influence these results, as the substrate material is breaking down and presumably this will occur over time. Two tests runs of 60 s were conducted with each of the higher density foams. Previously three test runs of 60 s were performed and in the case of the 15% density foam catalyst approximately eight test runs were conducted.

2.8.2 Compressed Powder Catalyst Bed Results

The two different grades of silver powder selected were tested in the chamber described previously. The length of the catalyst bed was focused upon in these tests to determine if an optimum length existed for each chamber diameter tested.

2.8.2.1 Test Results from the 9.7 mm Diameter Decomposition Chamber

The first set of tests was conducted using the chamber described, with a catalyst pack diameter of 9.7 mm. The coarse powder was tested initially and an example of the data recorded is shown in Figure 25, where the length of the bed tested was 10 mm.

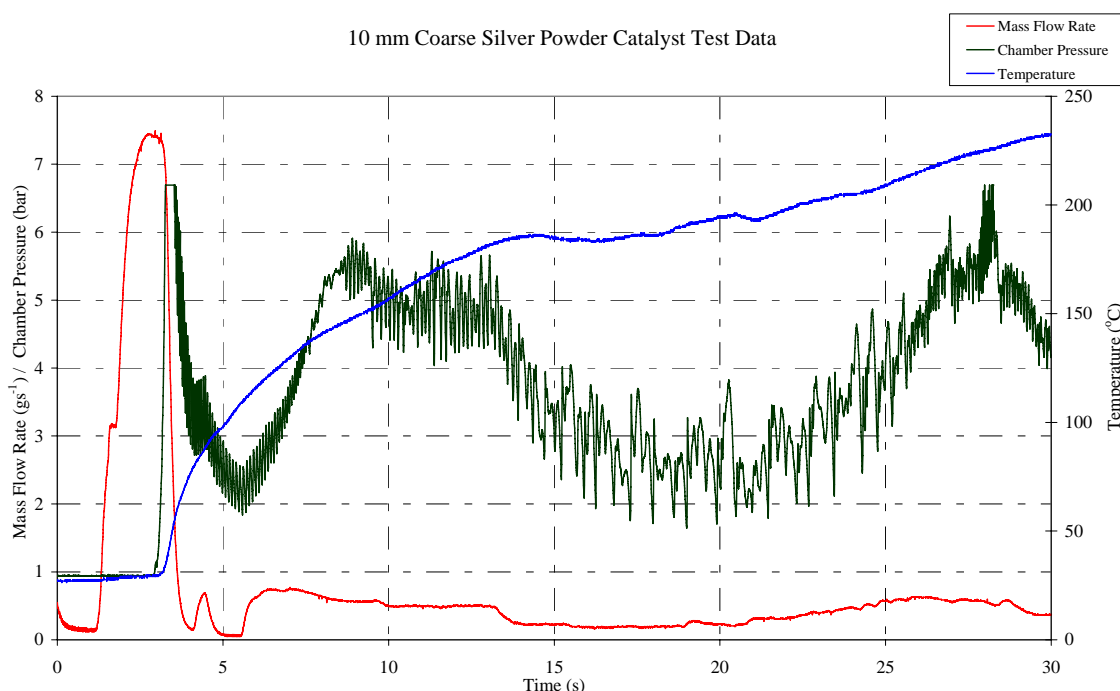


Figure 25: 10 mm Coarse Silver Catalyst Powder First Test Data

The propellant was pressurised to 4 bar and this remained fixed throughout the tests. The unsteady nature of this data indicated the need for a flow restrictor to further reduce the propellant flow rate upstream of the catalyst. This was initially achieved through the use of a Lee Visco Jet flow restrictor. The impact of this on performance is shown in Figure 26. The presence of the

flow restriction allows the decomposition to proceed smoothly with an excellent temperature profile resulting.

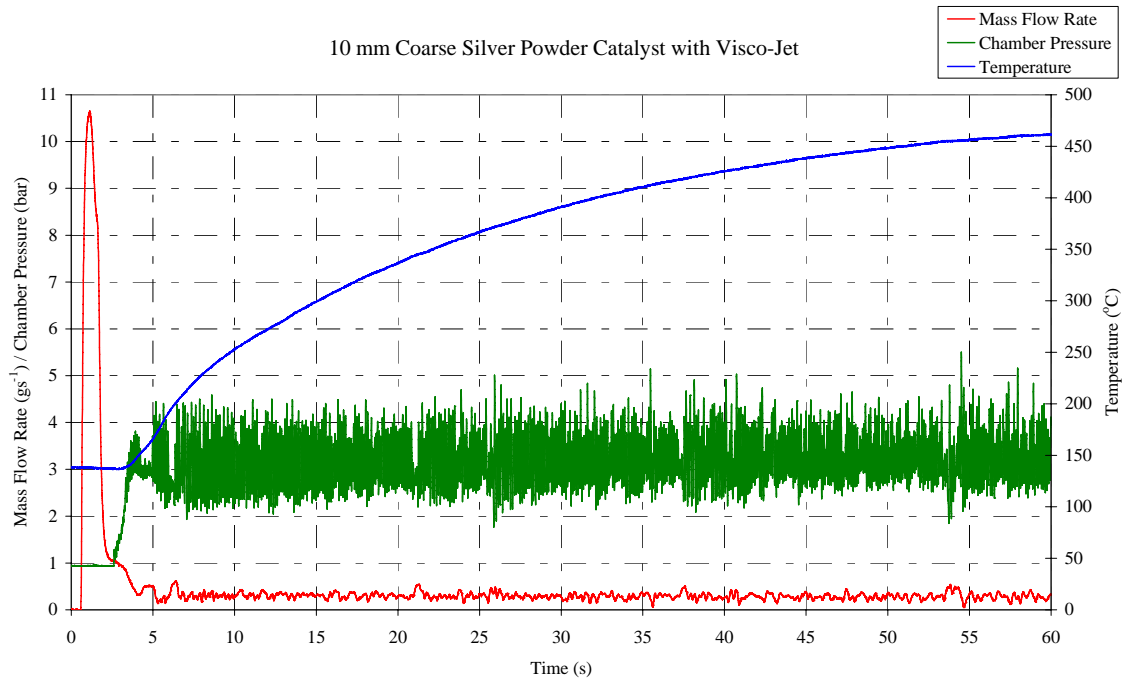


Figure 26: 10 mm Coarse Silver Powder Catalyst Test Data with Lee Visco Jet

A significant oscillation remained in the pressure trace indicating that the flow rate was still too high for the pack. To provide additional control to the propellant flow rate through the catalyst pack, the Visco Jet was replaced with a needle valve immediately upstream of the pack. This further improved the pressure and mass flow rate data as shown in Figure 27.

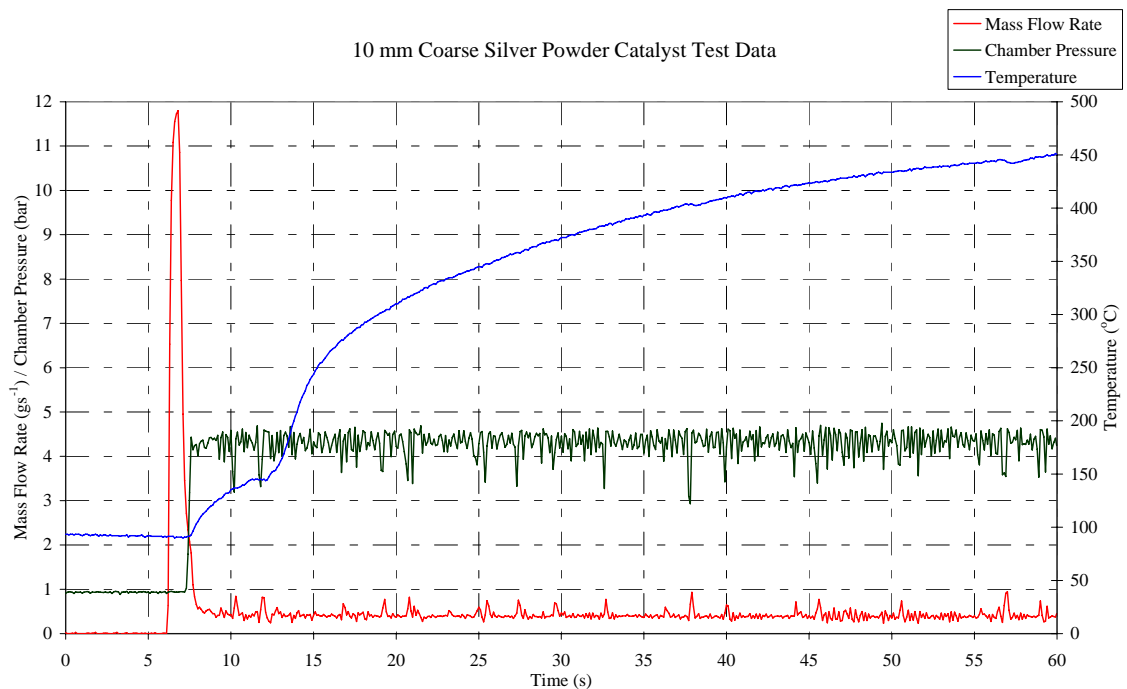


Figure 27: 10 mm Coarse Silver Powder Catalyst Test Data with Needle Valve

Following these adjustments to the test rig, the remainder of the testing proceeded. Four different lengths of catalyst were tested with the coarse grade of powder in the 9.7 mm diameter chamber and two lengths of the fine powder.

The coarse powder demonstrated a better decomposition characteristic overall. For each length of catalyst tested a temperature in excess of 450 °C was recorded together with high values of c^* . A summary of the data collected for the coarse powder catalyst in the 9.7 mm chamber is presented in Table 4, where the value of c^* was calculated using Equation 2 in each case.

Performance Characteristic	5 mm Catalyst	7.5 mm Catalyst	10 mm Catalyst	12.5 mm Catalyst
Chamber Pressure, p_c	4.12 bar	4.55 bar	4.20 bar	6.15 bar
Mass Flow Rate, \dot{m}	0.41 gs ⁻¹	0.41 gs ⁻¹	0.39 gs ⁻¹	0.59 gs ⁻¹
Decomposition Temperature, T_c	383 °C	456 °C	450 °C	423 °C
Effective Exhaust Velocity, c^*	791.84 ms ⁻¹	883.15 ms ⁻¹	857.02 ms ⁻¹	828.12 ms ⁻¹

Table 4: Data Summary of Coarse Silver Powder Catalyst Tests in 9.7 mm Diameter Chamber

Inspection of the data reveals that all of the tests produce values of c^* that are significantly higher than the theoretical maximum. For hydrogen peroxide at a concentration of 85%, this is 654 ms⁻¹. Inefficiencies in the measurements taken will contribute to this and in addition no allowance is made for the presence of a boundary layer within the throat of the thruster. The potential magnitude of this effect is discussed in more detail in section 4. Here, as the throat used for each test is the same, while the magnitude of c^* is high, the relative magnitude of c^* for the different configurations remains of interest. The value of c^* calculated for the 5 mm length case is an estimate as significant variations were evident in pressure data recorded for each test.

The pressure and mass flow rate data given in Table 4 are average values. The data traces for each of these characteristics contained oscillations, which are evident in the various figures shown. The oscillations observed in the 7.5 mm length case are the smallest in magnitude, indicating good decomposition, which is reflected in the highest value of c^* calculated.

Following tests with the coarse powder the fine silver powder was tested. An example of the data from a test run with a 10 mm length catalyst is shown in Figure 28. Overall the performance of the finer powder in the 9.7 mm diameter chamber appears comparable with that observed for the coarse silver powder, although a significant increase in the oscillations in the pressure and mass flow rate traces is evident. Two different lengths of catalyst bed were tested with the fine silver powder and a summary of the data collected is given in Table 5.

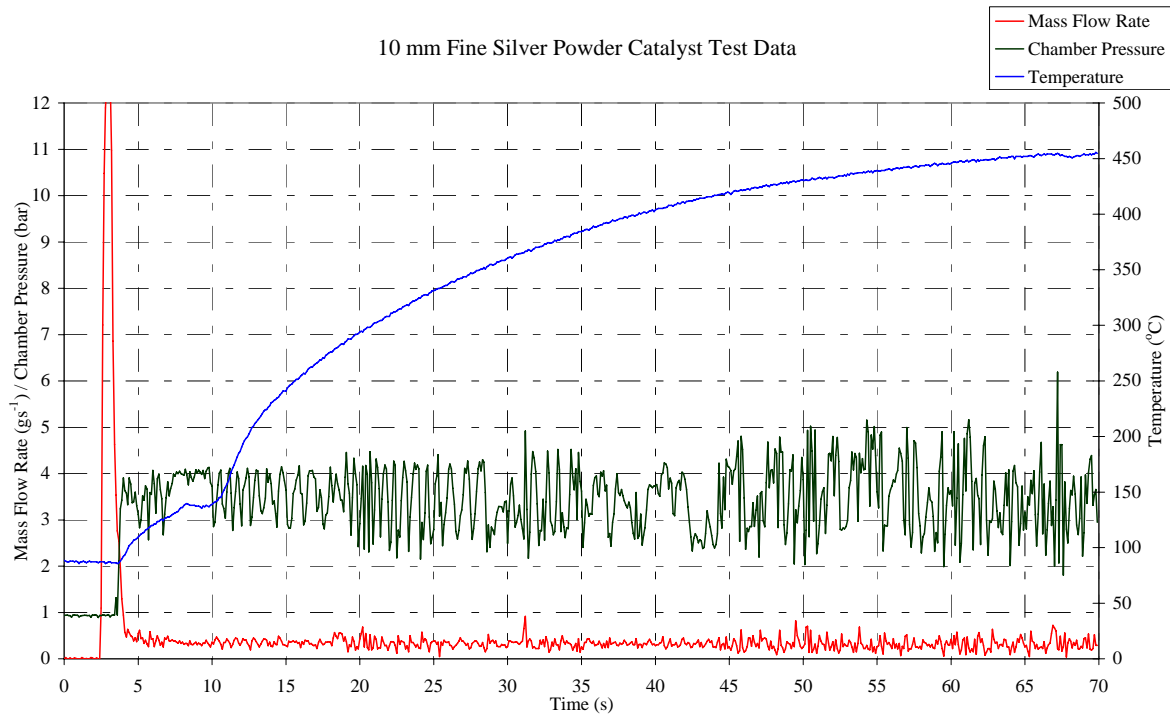


Figure 28: 10 mm Fine Silver Powder Catalyst Test Data

Performance Characteristic	7.5 mm Catalyst	10 mm Catalyst
Chamber Pressure, p_c	3.86 bar	3.49 bar
Mass Flow Rate, \dot{m}	0.35 gs^{-1}	0.33 gs^{-1}
Decomposition Temperature, T_c	460°C	455°C
Effective Exhaust Velocity, c^*	877.66 ms^{-1}	841.62 ms^{-1}

Table 5: Data Summary of Fine Silver Powder Catalyst Tests in the 9.7 mm Diameter Chamber

Reducing the length of the catalyst bed from 10 mm to 7.5 mm increased the frequency of the oscillations observed instead of decreasing them as observed for the coarse powder case. The smaller void space between the catalyst grains is thought to be responsible for this. The extent of the oscillations observed in combination with a limited supply of propellant led to the decision to cancel additional tests with this catalyst in the 9.7 mm chamber.

2.8.2.2 Test Results from the 7.7 mm Diameter Decomposition Chamber

The tests for the 7.7 mm diameter chamber were conducted using three different lengths of collar: 5 mm, 7.5 mm and 10 mm. Both powders were tested with all three lengths of catalyst bed and the performance observed was strikingly different for the two cases. The coarse powder exhibited a poor decomposition characteristic overall, with the temperature reaching a maximum of 380°C . The pressure trace was generally unstable allowing c^* to be calculated in only one case, the value of which demonstrates the poor performance observed. A summary of the data collected is presented in Table 6.

Performance Characteristic	5 mm Catalyst	7.5 mm Catalyst	10 mm Catalyst
Chamber Pressure, p_c	unsteady	2.55 bar	unsteady
Mass Flow Rate, \dot{m}	0.46 gs ⁻¹	0.33 gs ⁻¹	0.463 gs ⁻¹
Decomposition Temperature, T_c	300 °C	340 °C	380 °C
Effective Exhaust Velocity, c^*	-	614.94 ms ⁻¹	-

Table 6: Data Summary of Coarse Silver Powder Catalyst Tests in 7.7 mm Diameter Chamber

In contrast, the tests using the fine powder generated excellent results with temperatures in excess of 500 °C achieved, although oscillations remained in the pressure data. An example of the data generated is shown in Figure 29. The mass flow rate trace is not included in this chart as it was recorded using the mass balance arrangement described in section 2.7.3 and an average value was calculated.

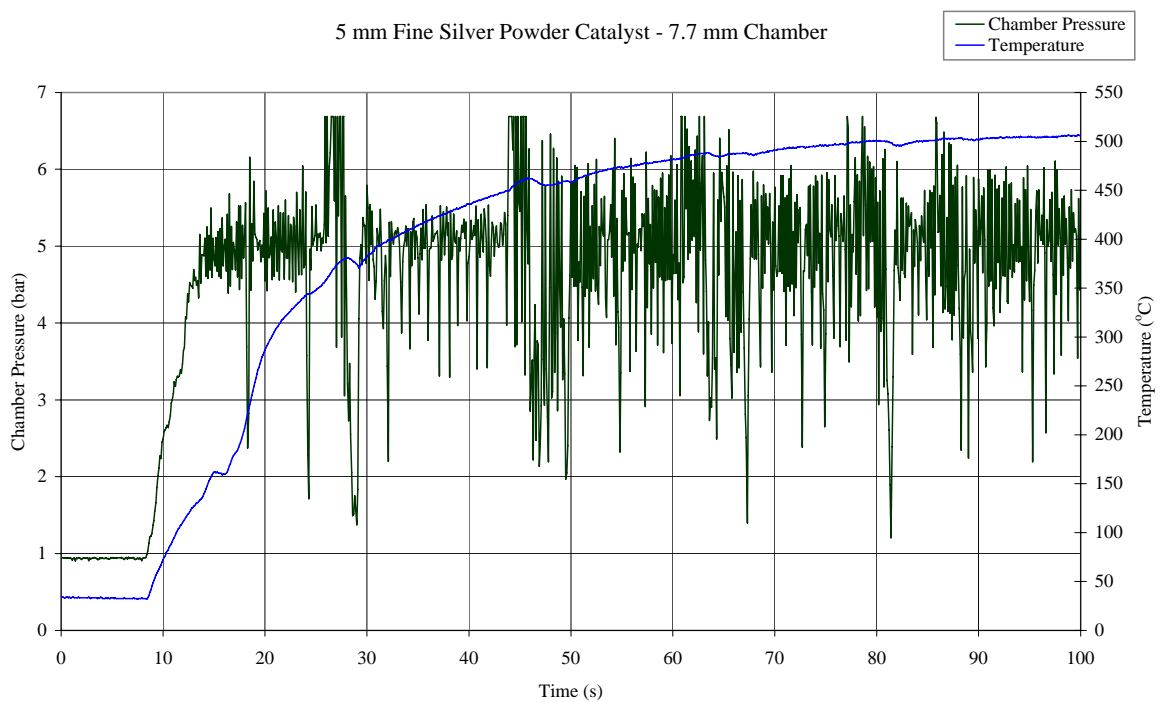


Figure 29: 5 mm Fine Silver Powder Catalyst Data in the 7.7 mm Diameter Chamber

Performance Characteristic	5 mm Catalyst	7.5 mm Catalyst	10 mm Catalyst
Chamber Pressure, p_c	4.9 bar	4.5 bar	4.6 bar
Mass Flow Rate, \dot{m}	0.43 gs ⁻¹	0.41 gs ⁻¹	0.44 gs ⁻¹
Decomposition Temperature, T_c	505 °C	485 °C	490 °C
Effective Exhaust Velocity, c^*	906.85 ms ⁻¹	873.44 ms ⁻¹	831.98 ms ⁻¹

Table 7: Data Summary of Fine Silver Powder Catalyst Tests in 7.7 mm Diameter Chamber

2.8.2.3 Test Results for the 6.7 mm Diameter Decomposition Chamber

Due to the instabilities observed using the coarse powder in the 7.7 mm diameter decomposition chamber, it was decided that only the fine powder would be tested in the 6.7 mm diameter decomposition chamber. Three lengths of catalyst bed were tested: 5 mm, 7.5 mm and 10 mm. Overall the severe pressure oscillations observed in previous cases remained present. The

temperature profiles recorded were encouraging, with temperatures of 500 °C registered. An example of the data recorded for a 5 mm length catalyst bed is shown in Figure 30. It can be seen that a good temperature profile exists, but the pressure reading remains oscillatory. The pressure transducer used was unable to record all of the data as it was rated to 6 bar.

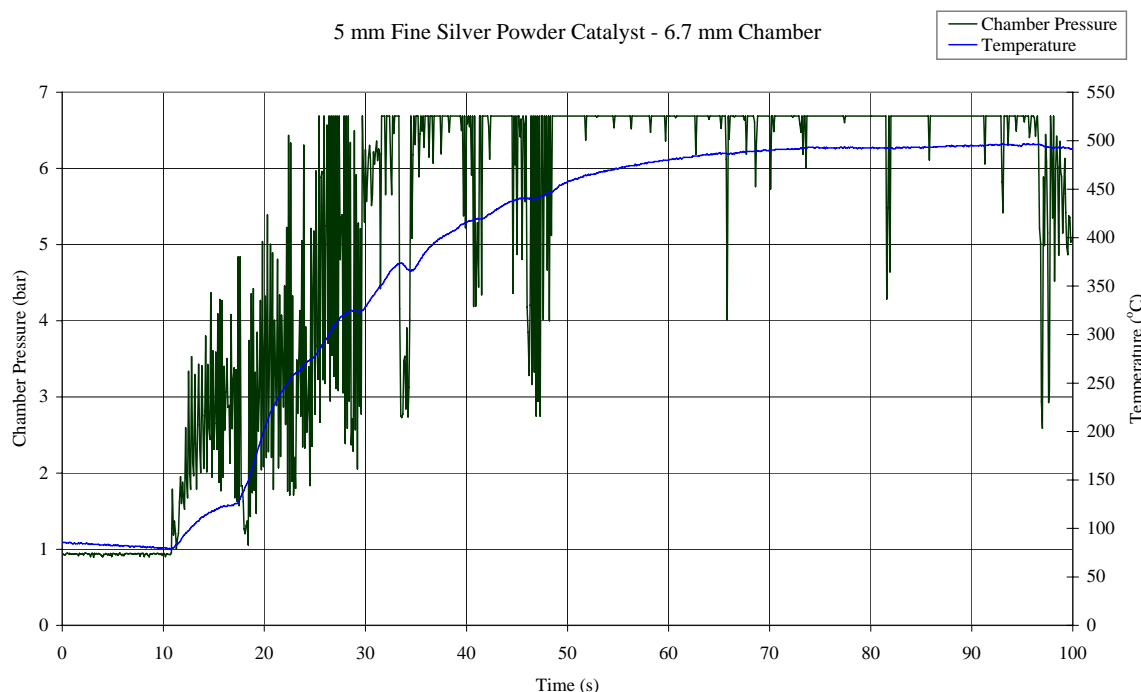


Figure 30: 5 mm Fine Silver Powder Catalyst Data in the 6.7 mm Diameter Chamber

2.8.3 Conclusions

There is evidence in the literature that the method of production of a manganese oxide catalyst has a significant impact on the activity observed [Ivanova'02]. The impact of this is clear from the changes in the catalyst loading observed using different methods. It was unfortunate that a change in the chilled environment led to the initial deposition method no longer being successful. It was at this point that the flash vaporisation technique was developed, however the uneven deposition led to significant reductions in performance observed. While the manganese oxide catalyst exhibits a high activity with hydrogen peroxide, it is clear that a more reliable deposition method is required to ensure a minimum level of catalyst loading. Once this is achieved, more testing may be considered in order to optimise the performance of the decomposition reaction.

The silver powder catalyst beds exhibited repeatable stable decomposition. It is difficult to determine the optimum geometry of the catalyst, however the shorter beds produced the highest temperatures indicating that a length to diameter ratio of less than 1 is optimal. The key conclusion from this work is that the silver powder reliably decomposed hydrogen peroxide flowing at a rate of 0.6 gs^{-1} in a chamber that contained a catalyst bed that was 6.7 mm in diameter

and 5 mm in length. It is thought that addition of insulation to the chamber will increase the temperature start-up characteristic and maximum temperature achieved. The catalyst bed also demonstrated cold-start capability, with some of the tests being conducted with an ambient temperature of 0 °C and a propellant temperature of 4 °C.

It is thought that the test set up itself contributed to the oscillations observed in the chamber pressure readings. Additional testing with an optimised test set up would confirm this.

There was insufficient time available to develop a test chamber using silicon as the structural material. The thermal losses encountered by the steel chamber used indicate that silicon would increase these losses significantly. In addition it is unlikely that a decomposition chamber with suitable dimensions could be created from silicon. It has been shown that a length to diameter ratio of less than 1 produces improved performance and the inherently flat geometries available with MEMS manufacturing methods is likely to preclude this from being possible.

3 Heat Transfer

The heat transfer characteristics of a thruster are critical to the performance. It may be shown that the exhaust velocity is directly proportional to the temperature in the combustion/decomposition chamber. The efficiency of the chemical reaction that enables the production of the hot gases is dependent upon various factors, which include the geometry of the combustion chamber. In particular the length and volume of the chamber are important to ensure there is enough time for the reaction to completed before the gases are expelled. The cube-square law that links volume and surface area means that as the dimensions of the combustion chamber are reduced the associated volume reduces at a higher rate than the length. This could lead to insufficient volume being available within the chamber thereby preventing the gases expanding properly and leading to premature discharge of the exhaust gases. Consideration of this effect at the design stage will allow the appropriate volume to result, however the heat transfer characteristics also require attention.

3.1 Prediction of Thermal Losses

The cube-square law indicates that a volume will rapidly reduce with miniaturisation, however the associated surface area reduces at a slower rate. The result is that there is less volume available to generate heat and more surface area available to transfer the heat away. To investigate this further models were developed and evaluated using Fluent®. Figure 31 illustrates the scale of the models

used and Table 8 summarises the results of a model created to investigate the miniaturisation of a heated cube.

Characteristic Length	20 mm	10 mm	5 mm	2.5 mm
Volume	$8 \times 10^{-6} \text{ m}^3$	$1 \times 10^{-6} \text{ m}^3$	$1.25 \times 10^{-7} \text{ m}^3$	$1.56 \times 10^{-8} \text{ m}^3$
Surface Area	$2.4 \times 10^{-3} \text{ m}^2$	$6 \times 10^{-4} \text{ m}^2$	$1.5 \times 10^{-4} \text{ m}^2$	$3.65 \times 10^{-5} \text{ m}^2$
SA/Volume Ratio	300	600	1200	2400
Total Exterior Heat Transfer per Unit Surface Area	$4.05 \times 10^4 \text{ Wm}^{-2}$	$8.10 \times 10^4 \text{ Wm}^{-2}$	$1.61 \times 10^5 \text{ Wm}^{-2}$	$3.09 \times 10^5 \text{ Wm}^{-2}$

Table 8: Heat Transfer Data

The model was assumed to be a block of solid stainless steel 316, at the centre of which was located a heat source that maintained at a constant temperature of 873 K. The physical properties of the steel used are summarised in Table 9.

Property	Value
Density	7960 kgm^{-3}
Specific Heat Capacity	$500 \text{ Jkg}^{-1}\text{K}^{-1}$
Thermal Conductivity	$16.3 \text{ Wm}^{-1}\text{K}^{-1}$

Table 9: Physical Properties of 316 Stainless Steel

Radiation boundary conditions were applied to the external surfaces, but convection was neglected thereby simulating a space environment. From the tabulated results it is possible to see that the heat transfer through the surface increases by a factor of two as the characteristic length is halved. This is same pattern that the surface area to volume ratio exhibits.

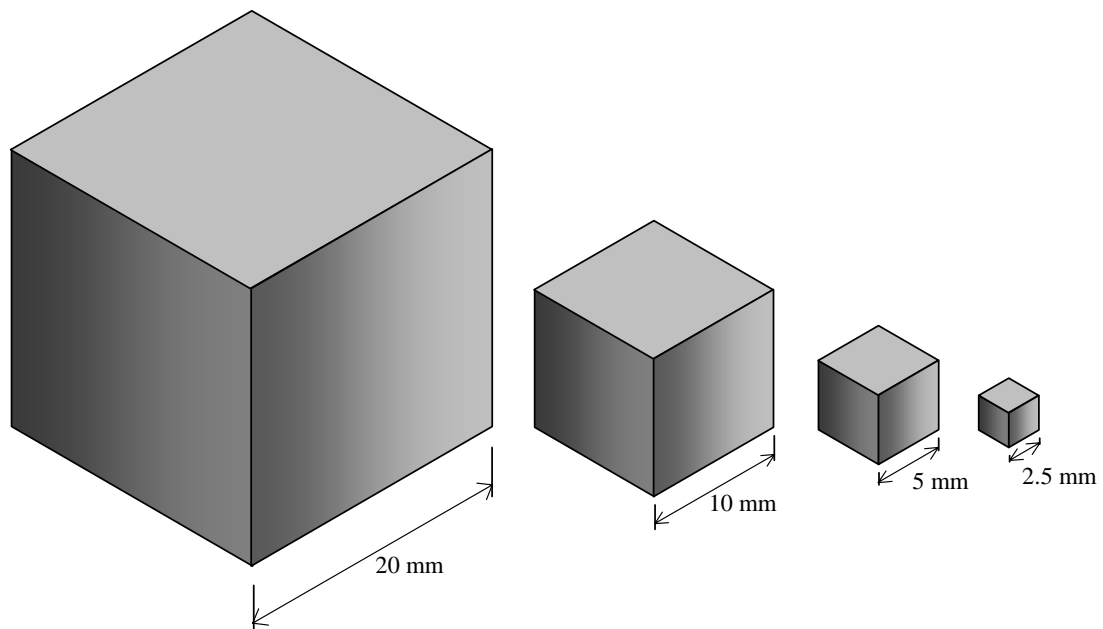


Figure 31: The Effect of Characteristic Dimension on Heat Transfer

The implications of this become more pronounced when the heat transfer through the wall is also considered. In a conventional scale thruster the wall thickness of the chamber is negligible in

comparison to the overall diameter. As the chamber reduces in size the wall thickness reaches a finite minimum dictated by physical constraints. At this point heat conduction through the wall then requires consideration, as it may no longer be considered to be insignificant.

3.1.1 Thermal Losses from a Steel Decomposition Chamber

To examine this effect in more detail a new model was created to simulate the combustion chamber of a thruster also using Fluent[®]. Due to the symmetry present within a cylinder, a model utilising a quarter section of the chamber was generated to minimise computing time. A wire-frame sketch of the model geometry used is shown in Figure 32.

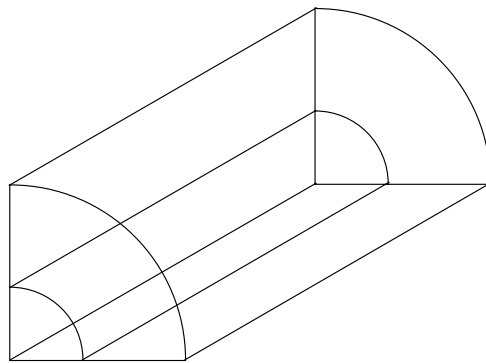


Figure 32: Wire-Frame Schematic of Cylinder Geometry

The outer section is the wall of the cylinder, assumed to be stainless steel and has a thickness maintained at 1.5 mm. The inner section is the open chamber, where the combustion would occur. For this analysis, where the steady state characteristics were of interest, it was appropriate to model this region as a solid section, which was maintained at a constant temperature of 873 K. A radiative boundary condition was applied to the exterior surface of the wall and symmetry conditions were applied to the symmetry lines. The emissivity, ϵ , of the exterior surface of the steel was assumed to be constant at 0.58. In reality this value will change with the temperature, however it was decided that as steady state operation was of interest a constant value was sufficient. The exterior temperature was assumed to be 4 K.

A series of models was created based upon this geometry, with the external diameter of the model varying from 6.5 mm to 26 mm. The steady-state solution of each model was considered and a typical conduction profile was observed. The range of models created allowed the effect of the constant wall thickness to be observed directly, as illustrated by Figure 33, where the total diameter of the model reduces from left to right. As the diameter of the model reduces, the wall thickness becomes larger relative to the internal diameter of the section and the temperature range observed increases. The exterior surface temperature is seen to reduce as the overall diameter reduces, indicating the wall is beginning to insulate the chamber.

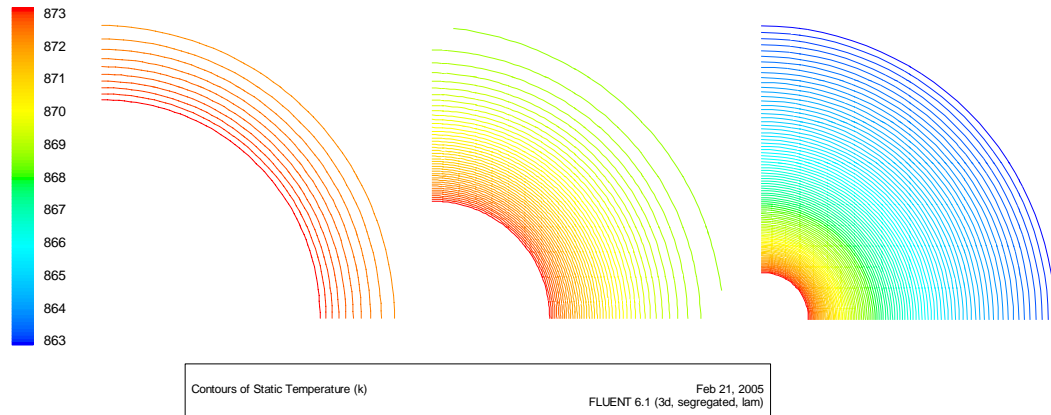


Figure 33: Thermal Contours Through Wall Thickness

The rate at which the heat is leaving the surface of the cylinder was then considered. Figure 34 shows the heat flux per unit surface area as a function of external diameter. The data reveals that the heat flux across the exterior surface increases as the relative wall thickness increases. This confirms that while the external surface is at a lower temperature, the increase in the surface area to volume ratio results in additional heat loss.

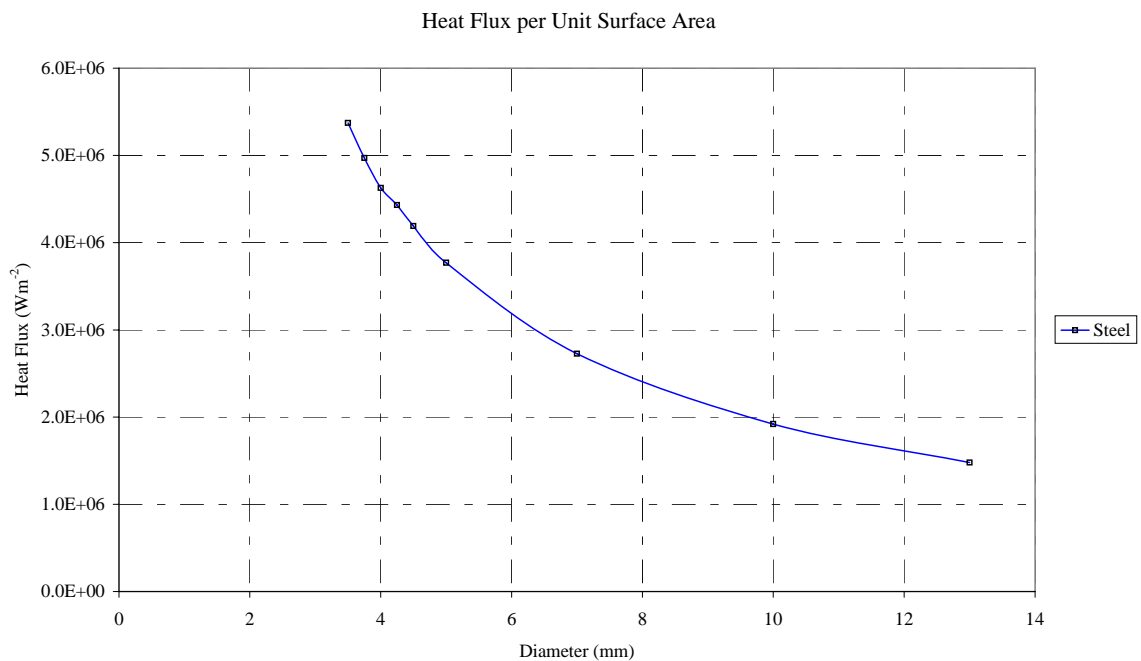


Figure 34: External Surface Heat Flux per Unit Area with Diameter

3.1.2 Assessment of Other Materials

The results in section 3.1.1 indicate that heat transfer is a key factor when considering the miniaturisation of a combustion chamber. The materials that the thruster itself is constructed from will have also a significant impact on the thermal characteristics. At conventional scales the maximum working temperatures of materials are considered to prevent failure in operation,

however heat loss is less of a concern. Here the thermal conductivity and heat capacity of the material are key material characteristics to consider. This is of particular importance when considering the use of MEMS technologies to miniaturise the system. The crystalline structure of silicon leads to a high thermal conductivity and in addition it has a high specific heat capacity, which allows it to store a large amount of energy within its bulk. The combination of these two effects means that the material will quickly draw heat away from the reaction, while taking a long time to reach an equilibrium point. In contrast a material such as steel has a significantly lower thermal conductivity and specific heat. This reduces the rate at which the combustion chamber accumulates energy and allows it to retain more of the energy released by the reaction.

Material	Macor [®]	Silicon
Density	2520 kgm ⁻³	2330 kgm ⁻³
Specific Heat Capacity	790 Jkg ⁻¹ K ⁻¹	705 Jkg ⁻¹ K ⁻¹
Thermal Conductivity	1.46 Wm ⁻¹ K ⁻¹	148 Wm ⁻¹ K ⁻¹

Table 10: Physical Properties of Macor[®] and Silicon

To assess the impact of this, two additional materials were considered, silicon and Macor[®]. Macor[®] was selected as it is a machinable ceramic, which may be suitable for use either as the structural material for the decomposition chamber, or as an insulating material. For this analysis the emissivity of silicon was assumed to be 0.5 and the emissivity of Macor[®] to be 0.77. The physical properties of these materials are summarised in Table 10.

	Steel		Macor [®]		Silicon	
Diameter (mm)	Tsurf (K)	Flux per Unit Surface Area (Wm ⁻²)	Tsurf (K)	Flux per Unit Surface Area (Wm ⁻²)	Tsurf (K)	Flux per Unit Surface Area (Wm ⁻²)
13	870.75	1.48E+06	847.21	1.73E+06	872.57	1.27E+06
10	870.36	1.92E+06	845.9	2.23E+06	872.22	1.64E+06
7	869.30	2.73E+06	842.87	3.15E+06	871.36	2.34E+06
5	866.60	3.77E+06	836.68	4.28E+06	868.95	3.25E+06
4.5	866.86	4.19E+06	834.87	4.71E+06	869.42	3.60E+06
4.25	866.43	4.43E+06	833.08	4.95E+06	869.10	3.82E+06
4	862.64	4.63E+06	828.07	5.12E+06	865.33	4.09E+06
3.75	863.35	4.97E+06	826.08	5.42E+06	866.40	4.33E+06
3.5	864.42	5.37E+06	822.71	5.74E+06	867.92	4.59E+06

Table 11: Data Summary of Heat Flux Models

The high thermal conductivity of silicon led to external surface temperature for each diameter modelled being higher than for both steel and Macor[®]. The total energy lost from the exterior surface of the model was predicted to be the lowest for the silicon cases as the low emissivity reduces the heat flux. The impact of different materials on the above analysis was considered and the results are summarised in Table 11.

This is illustrated further by Figure 35, which shows the heat flux trend for each material. Based upon the emissivity values used this result is expected. If the emissivity of Macor[®] was reduced through the application of a paint, or heat shield then the results would be more favourable.

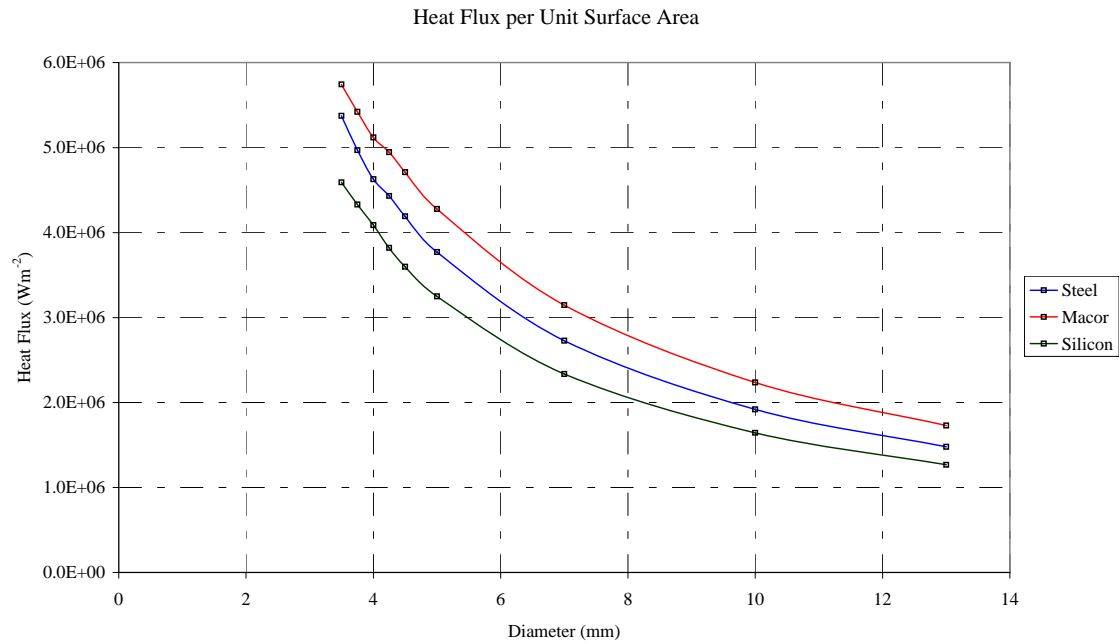


Figure 35: External Heat Flux per Unit Surface Area Materials Comparison

3.2 Conclusions

The thermal characteristics of a thruster are central to the resultant performance. The low mass flow rates of propellant used in a microthruster will result in less energy being released, therefore containment of the energy is critical. The high surface area to volume ratio of a microthruster exacerbates the thermal losses, reducing the overall performance. These models have demonstrated that any additional mass increases the thermal losses. The material to be used in the construction must have high structural integrity but be able to withstand the extreme temperature range to which it will be subjected and be capable of being machined accurately. Three different materials were investigated, stainless steel 316, Macor[®] and silicon. The models suggest that the high specific heat capacity of Macor[®] will increase thermal losses under steady state conditions. In addition the high thermal conductivity of silicon will lead to energy quickly being absorbed into the bulk material. Thus it is concluded that the chamber should be machined from a material such as stainless steel for ease of manufacture and strength, but a heat shield should be included in the design to reflect radiated heat back into the thruster.

4 Nozzle Flow

This section will summarise the work completed that relates to the miniaturisation of an exhaust nozzle. The isentropic theory relating to the performance of a nozzle will be introduced to enable

a performance evaluation of the models created. The complete development of the flow within a nozzle is investigated through the use of numerical models. These enable the evaluation of the performance of a nozzle as it reduces in dimension.

4.1 Isentropic Nozzle Theory

The purpose of the exhaust nozzle is to expand and accelerate the hot gases produced upstream, thereby generating thrust with minimal loss. Use of isentropic theory enables the design of an ideal nozzle, which expands the exhaust gas perfectly. The condition of perfect expansion may be shown to occur when the pressure of the exhaust gas at the exit plane of the nozzle is equal to that of the ambient environment. For a rocket nozzle operating in the vacuum of space this is possible in theory, but impractical to achieve as the nozzle length required to expand the gas becomes excessive. To address this a pressure ratio is used, which relates the chamber pressure to the exit pressure, p_c/p_e . The magnitude of this ratio is different for different types of rocket engine. Typically for a monopropellant engine it should be approximately 65.

4.1.1 Nozzle Performance Evaluation

The performance of the decomposition chamber was characterised previously using the effective exhaust velocity, c^* . This allowed evaluation of the efficiency of the chamber without consideration of the nozzle. The performance of a nozzle is usually evaluated through use of the thrust coefficient, c_f , which is a measure of measure of nozzle effectiveness. The value provides an indication of how the presence of the nozzle magnifies the thrust generated. It is defined by Equation 6 [Hill'92] with respect to thrust, \mathcal{T} , chamber pressure, p_c and throat area, A^* . An alternative definition is also possible for the ideal rocket case where it may be derived as a function of the pressure ratio, p_c/p_e and the ratio of specific heats, γ , given in Equation 7 [Hill'92].

$$c_f \equiv \frac{\mathcal{T}}{p_c A^*}$$

Equation 6: Definition of the Thrust Coefficient

$$c_f = \sqrt{\left(\frac{2\gamma^2}{\gamma-1}\right)\left(\frac{2}{\gamma+1}\right)^{\frac{\gamma+1}{\gamma-1}}\left[1-\left(\frac{p_e}{p_c}\right)^{\frac{\gamma-1}{\gamma}}\right]} + \frac{(p_e - p_a)A_e}{p_c A^*}$$

Equation 7: Thrust Coefficient for the Ideal Rocket

This second equation demonstrates that for the ideal case the thrust coefficient is a function of the nozzle geometry only. The pressure term can be regarded as a measure of the nozzle efficiency with respect to the actual pressure ratio. A theoretical value of c_f may be calculated from Equation 7 for a given pressure ratio. To calculate a value for c_f that is valid for a real nozzle an alternative approach is required. The thrust generated by a rocket engine may be defined as a function of the mass flow rate of propellant, \dot{m} and the effective exhaust velocity, u_{eff} as shown in Equation 8.

$$T = \dot{m}u_{eff}$$

Equation 8: Thrust as a Function of Mass Flow Rate and Effective Exhaust Velocity

This may be combined with Equation 6 and Equation 2 to give an empirical definition of the thrust coefficient, given in Equation 9.

$$c_f = \frac{u_{eff}}{c^*}$$

Equation 9: Empirical Definition of the Thrust Coefficient

A value of c_f may be calculated using Equation 9 in combination with velocity data from numerical models. The ideal value of c_f can then be compared with this prediction to provide an indication of the efficiency of the nozzle.

4.1.2 Geometric Parameters

The design of a rocket nozzle is based upon thermodynamic relations, which describe the expansion of a perfect gas. These are used to develop the geometric parameters required to size the nozzle.

The first parameter calculated is the mass flow rate. The definition of the thrust coefficient, given in Equation 6 may be combined with that of, c^* , given in Equation 2 to generate an equation for thrust as shown in Equation 10. Using empirical values for both c^* and c_f the required mass flow rate for a given magnitude of thrust can be calculated.

$$T = \dot{m}c^*c_f$$

Equation 10: Thrust as a Function of c^* and c_f

Knowledge of the mass flow rate together with the conditions within the decomposition chamber enables calculation of the throat area required to generate supersonic flow using Equation 2.

The expansion of the flow is the next consideration. The pressure ratio, p_c/p_e , defines the degree to which the flow is expanded and the rate at which this occurs is defined by the area ratio, A^*/A_e .

This ratio is defined in Equation 11, where γ , is the ratio of specific heats of the exhaust products [Sutton'01]. The derivation of this equation is based upon the pressure ratio, P_e/P_c , and the assumption that the flow will become supersonic at the throat of the nozzle.

$$\frac{A^*}{A_e} = \left(\frac{\gamma+1}{2} \right)^{\frac{1}{\gamma-1}} \left(\frac{p_e}{p_c} \right)^{\frac{1}{\gamma}} \sqrt{\left(\frac{\gamma+1}{\gamma-1} \right) \left[1 - \left(\frac{p_e}{p_c} \right)^{\frac{\gamma-1}{\gamma}} \right]}$$

Equation 11: Area Ratio Definition [Sutton'01]

Knowledge of the area ratio in combination with the throat area allows calculation of the required exit area of the nozzle as shown in Equation 12.

$$A_e = \left(\frac{A^*}{A_e} \right)^{-1} A^*$$

Equation 12: Exit Area Calculation

The length of nozzle required to expand the flow sufficiently is calculated using Equation 13, where α is the expansion half angle of the nozzle [Hill'92].

$$L_n = \frac{d^* \sqrt{\frac{A_e}{A^*} - 1}}{2 \tan \alpha}$$

Equation 13: Nozzle Length

4.2 Nozzle Inefficiencies

Various inefficiencies may degrade the performance of a nozzle. In particular the development of a boundary layer will modify the behaviour of a flow. A boundary layer will develop where a fluid is flowing beside a solid surface. Within a nozzle a boundary layer can significantly reduce the volume available for the expansion of the flow. The classification of a boundary layer is considered here together with the numerical methods used to describe the velocity distribution within it.

4.2.1 Types of Boundary Layer

A fluid flow is classified as laminar, turbulent or transitional and the same classification extends to boundary layers. A laminar boundary layer is a smooth layer, which contains all the effects of fluid viscosity. A severe velocity gradient exists and little mixing occurs within the fluid, leading to high shear stresses within the fluid. In comparison within a turbulent boundary layer the fluid is no longer held into structured layers. Instead a series of small vortices is formed allowing the

fluid to rotate. This leads to convective mixing between the fluid adjacent to the wall and the freestream flow, reducing the shear stresses observed. A transitional boundary layer encompasses elements of both laminar and turbulent boundary layers.

The flow through the exhaust nozzle will be turbulent initially following exit from the decomposition chamber and as the flow passes through the nozzle it will become supersonic. The low Reynolds number of the flow implies that it will quickly become laminar following exit from the decomposition chamber. The acceleration of the flow through the nozzle may cause the flow to become turbulent again therefore to ensure correct representation of the flow a turbulent flow is considered. The turbulent boundary layer will now be considered in more detail.

4.2.2 Structure of a Turbulent Boundary Layer

A turbulent boundary layer is thought to consist of three regions: one close to the wall, one close to the freestream fluid and one between the two. The viscosity effects are restricted to the layer close to the wall, the viscous sublayer, which is significantly thinner than the complete boundary layer. The viscous sublayer exhibits behaviour that is similar to that of a laminar boundary layer with a laminar velocity profile and viscosity dominated flow. The exterior layer is called the overlap layer, as this accounts for the change between flow within and exterior to the boundary layer, the layer between the two is then called the buffer layer. The location of the different layers relative to each other and a wall is illustrated in Figure 36.

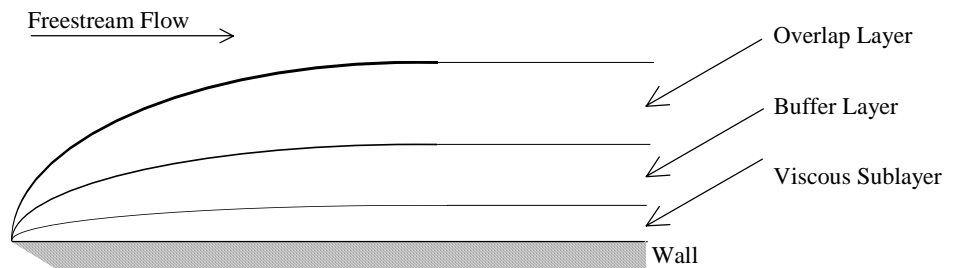


Figure 36: Turbulent Boundary Layer

The order of magnitude of the thickness of each of these layers varies considerably, with the thickness of the viscous sublayer appearing negligible in comparison to that of the overlap layer. It is impossible to ignore the presence of the viscous sublayer however, therefore a characteristic wall coordinate is introduced, y^+ , which stretches with y -coordinate. The definition of y^+ is given in Equation 14, where y is the distance from the wall and ν is the dynamic viscosity [Schlichting'00]. The friction velocity, u_τ , is defined in Equation 15, where $\bar{\tau}$ is the time averaged wall shear stress [Schlichting'00]. The y^+ coordinate is defined as function of distance away from the wall, hence at the wall $y^+ = 0$ and $du^+/dy^+ = 1$.

$$y^+ = \frac{yu_\tau}{\nu}$$

Equation 14: Definition of y^+

$$u_\tau = \sqrt{\frac{\tau_w}{\rho}}$$

Equation 15: Definition of Friction Velocity

This allows the velocity distribution in the boundary layer, u^+ , to be defined such that it remains valid throughout the different layers. Characterisation of a turbulent boundary layer is then possible through use of the y^+ coordinate as shown in Table 12 [Schlichting'00].

Viscous Sublayer	$0 \leq y^+ < 5$
Buffer Layer	$5 < y^+ < 70$
Overlap Layer	$70 < y^+$

Table 12: Turbulent Boundary Layer Characterisation

4.2.3 Boundary Layer Development

There are various conditions that will promote or inhibit the growth of a boundary layer, in particular the pressure gradient. An adverse pressure gradient, where the static pressure increases in the direction of the flow will inhibit the growth of a boundary layer. A favourable pressure gradient, where the static pressure decreases in the direction of the flow, will in contrast encourage the growth of a boundary layer. In the nozzle a favourable pressure gradient exists, as the flow is expanding, therefore a boundary layer develops causing a modification in the flow profile. The presence of the boundary layer will reduce the effectiveness of the nozzle, hence evaluation of the actual performance of the nozzle itself is possible though identification of the position and thickness of the boundary layer, δ .

The edge of the boundary layer may be determined in numerous ways although two are of particular interest and both relate to the flow velocity. The most common definition relates to the magnitude of the flow velocity. The edge of the boundary layer, where $y = \delta$, is defined as the point where the velocity within the boundary layer is 99% of the freestream velocity, giving the first condition shown in Equation 16 [Schlichting'00].

The presence of high velocity gradients within the boundary layer was noted previously with reference to the shear stresses. At the edge of the boundary layer the velocity gradient and associated shear stresses tend to zero as the flow is moving at the freestream velocity. This leads to the second condition given in Equation 16 [Schlichting'00].

$$y = \delta \quad \text{when} \quad u = 0.99u_{\infty} \quad \text{and} \quad \frac{du}{dy} = 0$$

Equation 16: Definition of the Edge of the Boundary Layer

4.2.4 Limitations of Classic Boundary Layer Theory

The theory outlined above is based upon empirical data that has been collected and analysed over the course of many years. The velocity of the flows involved is usually high and the characteristic dimensions large, leading to large Reynolds numbers and thin boundary layers. The limitations of this theory in relation to flows with low velocity and small characteristic dimensions are unknown. Flows with low Reynolds numbers have been investigated but uncertainty in the results has led to different conclusions [Hsieh'04, Mala'99]. In the absence of any other literature, throughout this analysis it was assumed that classic boundary layer theory was valid.

4.3 Development of Numerical Models

A series of models was created to investigate how the flow developing within a nozzle is modified as the dimensions of the nozzle reduce. The parameter selected to determine the size of the nozzle was the magnitude of thrust produced. Nine thrust levels were initially identified ranging from 500 mN to 1 mN. Four different types of geometry were investigated and the dimensions for each model were calculated based upon the theory summarised previously. A standard geometry was used as a baseline and the other models were created as modifications of this to allow continuity between the different aspects investigated. The literature revealed that there was little performance advantage from use of a contoured nozzle, hence a simple conical nozzle geometry was selected. The geometry of the model immediately upstream of the nozzle section remained identical in each case, with an inlet diameter of 5 mm and a convergence angle of 60°. The chamber pressure was assumed to be 5 bar in each case, although in practice optimisation of this would be required through experiment. The pressure ratio used was 65 and the value of the ratio of specific heats, γ , was taken to be 1.27 from characteristic data for the exhaust products of 85% concentration hydrogen peroxide.

The particular aspects of each different type of model are now discussed, with the initial geometry calculations outlined in the standard geometry section.

4.3.1 Standard Geometry

For each thrust level used, the mass flow rate, \dot{m} , required was calculated using Equation 10. Equation 7 was used to calculate c_f , using the parameters specified previously, giving $c_f = 1.68$.

The value for c^* was calculated from Equation 3 assuming a ratio of specific heats of the decomposition products, γ of 1.26, giving $c^* = 701 \text{ ms}^{-1}$.

Knowledge of the mass flow rate, \dot{m} , allowed the calculation of the throat area of the nozzle through use of Equation 2. The chamber pressure, p_c , was assumed to be 5 bar in all cases for ease of comparison, although in practice optimisation through experiment would be required. From the throat area the throat diameter was calculated using geometric relations.

The area ratio was calculated using Equation 11 in combination with the same value of γ as before, giving $A^*/A_e = 0.128$. The exit area of the nozzle was then calculated using Equation 12, followed by the exit diameter. Finally the length of the nozzle, L_n , was calculated using Equation 13, where α , was assumed to be 15° . A summary of the relevant dimensions for the nine models created is provided in Table 13 and a schematic of the geometry is shown in Figure 37.

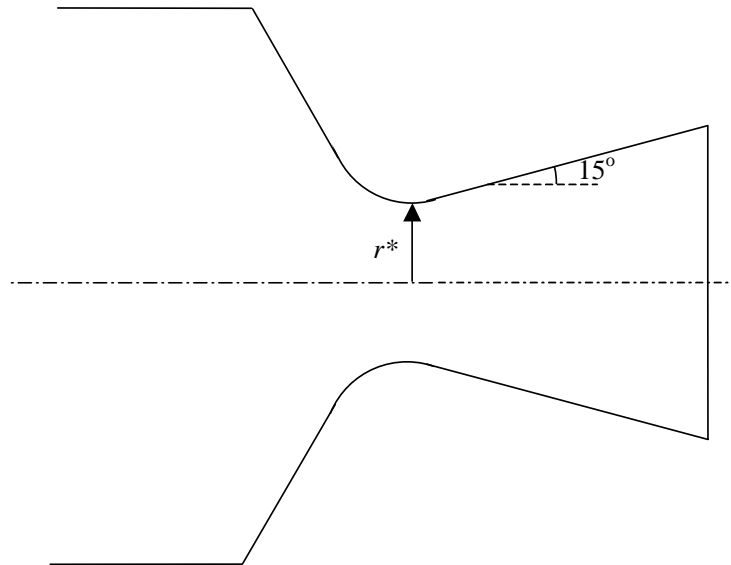


Figure 37: Schematic of the Standard Geometry

Model	A	B	C	D	E	F	G	H	I
\mathcal{T} (mN)	500	250	125	50	25	10	5	2.5	1
\dot{m} (gs^{-1})	0.425	0.212	0.106	0.042	2.12E-02	8.49E-03	4.25E-03	2.12E-03	8.49E-04
d^* (mm)	0.865	0.612	0.432	0.273	0.193	0.122	0.086	0.061	0.039
d_e (mm)	2.416	1.708	1.208	0.764	0.540	0.342	0.242	0.171	0.108
L_n (mm)	2.89	2.05	1.45	0.915	0.647	0.409	0.289	0.205	0.129

Table 13: Summary of Standard Nozzle Geometric Parameters

4.3.2 Wide Expansion Angle

The presence of a thick boundary layer, blocking a significant proportion of the nozzle is the key concern as the dimensions of a nozzle reduce. An alternative to using the standard geometry with

an expansion half-angle of 15° is to increase the expansion angle. The effect of this modification on the performance observed was investigated using this model, where α was increased by 5° from 15° to 20° . The area ratio used remained the same, hence the nozzle length reduced slightly to accommodate the increased expansion angle. Four of the nine basic thrust levels were selected for this analysis. The nozzle length dimensions used are summarised in Table 14 and the geometry is illustrated in Figure 38.

Model	A	E	G	I
Ln (mm)	2.13	0.476	0.213	0.095

Table 14: Length Parameters for Wide Expansion Angle Model

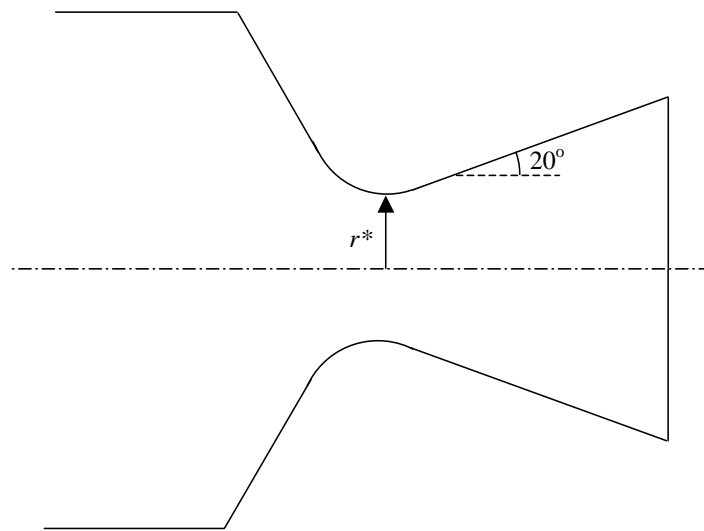


Figure 38: Schematic of the Wide Expansion Angle Geometry

4.3.3 Sharp Throat Profile

These models were based upon the same dimensions developed initially, however the throat contour was removed and replaced with a sharp throat. The creation of a perfectly smooth throat contour when the throat diameter is of the order of $50\text{ }\mu\text{m}$ would be difficult to achieve with current manufacturing techniques. A sharp throat will cause a modification to the flow profile observed, therefore these models were designed to allow the impact of this on the performance to be evaluated. Three of the four thrust levels selected previously were again used for these models and Figure 39 illustrates this geometry.

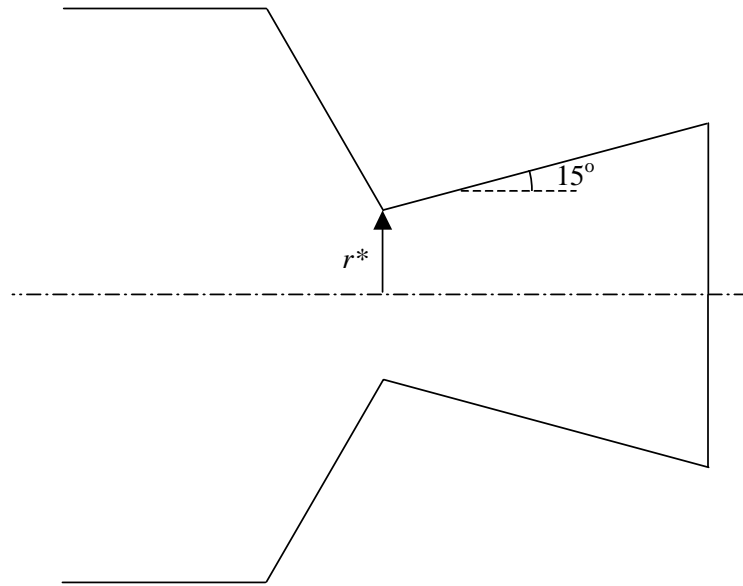


Figure 39: Schematic of the Sharp Throat Geometry

4.3.4 Convergent Section Only

The predicted presence of a thick boundary layer within the nozzle may result in the presence of the nozzle being of little advantage. To test this four models were created based upon four thrust levels, without the divergent section to evaluate the modification in performance observed. The initial throat curvature was retained to allow some straightening of the flow prior to exit, as illustrated by Figure 40.

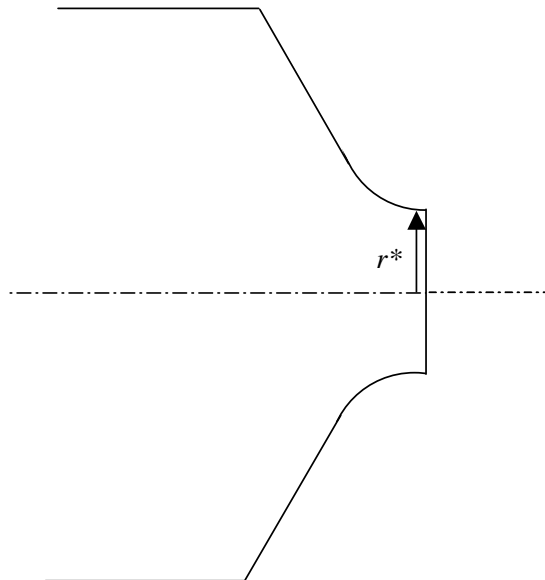


Figure 40: Schematic of the Convergent Section Only Geometry

4.4 Solution Methodology

The geometry for each of the models described was created and meshed using the standard pre-processor for Fluent®, Gambit. The geometry for each model was split into a number of sections to allow the mesh to be graded such that a fine mesh was present in the nozzle throat region. An example of a geometry without the mesh is shown in Figure 41. The colour scheme used by Gambit allows the colour of the lines and vertices to change dependent upon their function and connectivity. For example in the image shown the edge of the model is shown with orange lines, as these are only used once, whereas the interior sections shown with blue lines, as these are used twice. Each of the lines shown represents a boundary and each area represents a zone. The primary attributes of these are set in Gambit and then refined in Fluent®. For example a boundary can be set to represent a variety of features, including a wall, an interior, an inlet or an exit. The interior setting is of particular importance in these models as this means that it is in effect invisible to the flow.

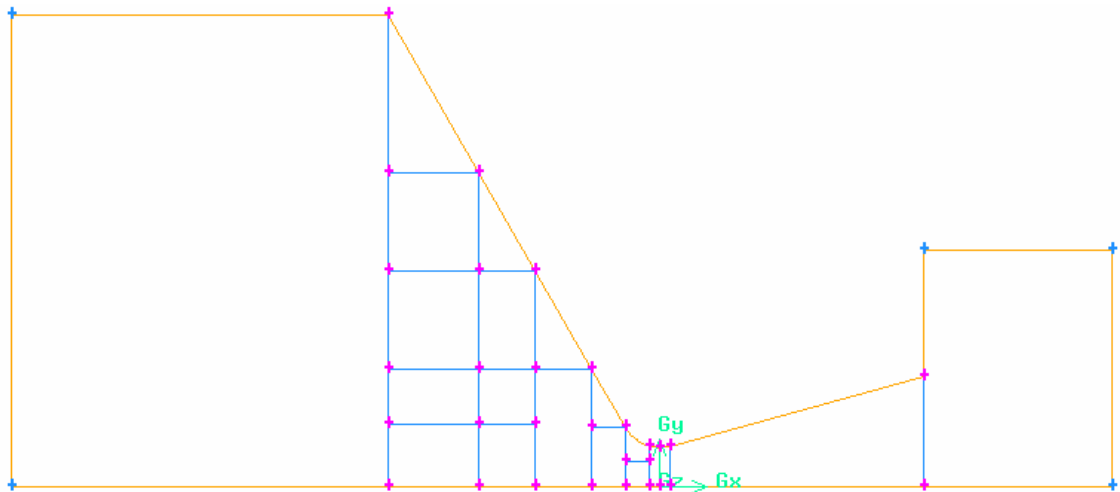


Figure 41: Standard Model Geometry

Following generation of the mesh, the geometry was then imported into Fluent® and additional parameters, including boundary conditions were defined. For each model the inlet boundary conditions were set to include a chamber pressure of 5 bar and freestream temperature of 873 K. In addition a pressure drop was applied across the inlet plane of the model to generate a flow velocity in the x-direction. The calculations used to generate the dimensions of the nozzle provided the mass flow rate for each case. From this the velocity required was calculated using Equation 17.

$$\dot{m} = \rho Au$$

Equation 17: The Continuity Equation

The velocity was transformed into a pressure drop input to increase the stability of the model. This was calculated through use of Equation 18, which is based upon Bernoulli's equation for incompressible fluid flow.

$$\Delta p = \frac{1}{2} \rho u^2$$

Equation 18: Pressure Drop Inlet Condition Calculation

The region of the model exterior to the nozzle was set to represent a space environment. To achieve this the pressure was set to zero pressure and the temperature to 4 K and the exit boundaries were set to be pressure outlets.

The material selected to flow through the nozzle in the simulation was based upon the hot exhaust products of the decomposition reaction. It was a mixture of water and oxygen, the parameters of which was calculated using a mass balance approach assuming complete decomposition of 85% concentration hydrogen peroxide. The material accounts for the high viscosity of the mixture, which is of particular interest when considering the boundary layer. The attributes of the material that were included are summarised in Table 15. The density of the fluid was assumed to be an ideal gas as the flow was expected to be supersonic.

Property	Value
Thermal Conductivity, k	$0.0547 \text{ Wm}^{-1}\text{K}^{-1}$
Specific Heat Capacity, c_p	$1596 \text{ Jkg}^{-1}\text{K}^{-1}$
Bulk Viscosity, μ	$3.06 \times 10^{-5} \text{ kgm}^{-1}\text{s}^{-1}$
Average Molecular Mass, \mathcal{M}	21.822

Table 15: Estimated Properties of the Exhaust Gas

Following definition of a model, the solution was initialised and solved using the 2-dimensional double precision, axi-symmetric, coupled, implicit solver combined with the k- ϵ turbulence model. To improve the stability of the solution, the standard k- ϵ model was used to generate the initial solution and this was changed to the realisable k- ϵ model for the final iteration run. In addition enhanced wall functions were used to ensure the correct treatment of the near-wall region, combined with a y^+ value of less than 5 to allow complete resolution of the boundary layer. Once initialised the solution was iterated until the residuals indicated a change of less than 10^{-3} in all cases.

4.4.1 Limitations of Numerical Modelling

When considering the results from these models the particular conditions applied in each region should be noted. This is of particular importance with reference to the region exterior to the nozzle, where the conditions were set to be a vacuum. The exhaust flow will quickly become rarefied under these conditions and the governing equations used by Fluent[®] are no longer valid.

The exterior region was included to ensure that the flow profile inside the nozzle was representative, however the data in this region itself is of little interest.

4.5 Presentation of Results

The results from each of the models created may be presented in a number of different formats dependent upon the particular aspects that are of interest. The various different forms of data presentation relevant to this research will be demonstrated to justify the reasoning for the approach used to evaluate the data generated.

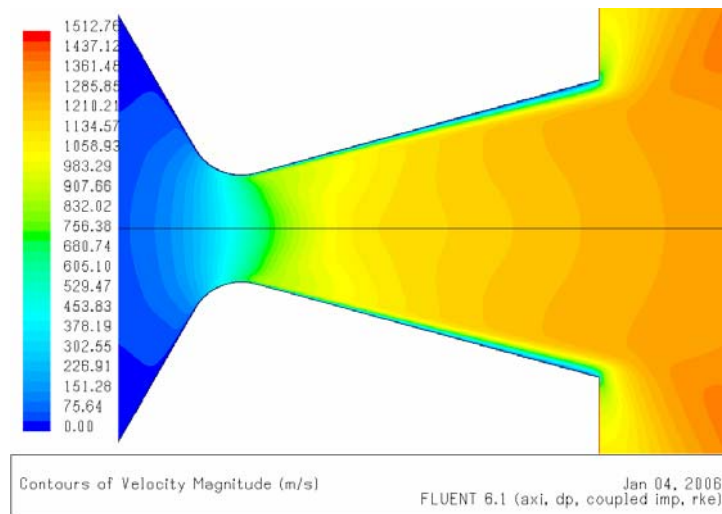


Figure 42: Contours of Velocity Magnitude

Contours of velocity magnitude within the nozzle may be displayed as illustrated in Figure 42. From this it is possible to identify the presence of a boundary layer within the divergent section of the nozzle reducing the divergence angle. The precise location of the edge of the boundary layer is difficult to determine exactly due to the cluster of contours present.

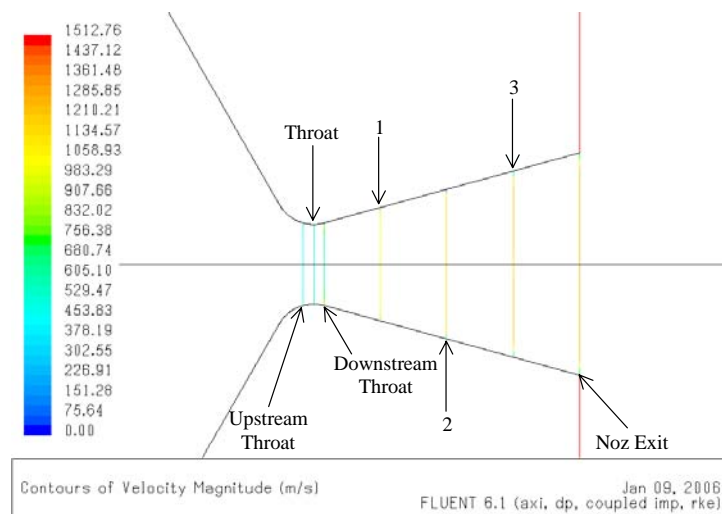


Figure 43: Location of Sample Planes

The first three sample planes (Upstream Throat, Throat and Downstream Throat) are clustered around the throat to allow a better resolution of the boundary layer development. The remaining planes (1, 2, 3 and Noz Exit) are then spaced equidistant throughout the length of the nozzle with the last located at the exit plane of the nozzle. The velocity data relating to the six sample planes shown are illustrated in Figure 44. The yellow and blue traces represent the velocity profiles immediately adjacent to the nozzle throat and share the same maximum radial coordinate.

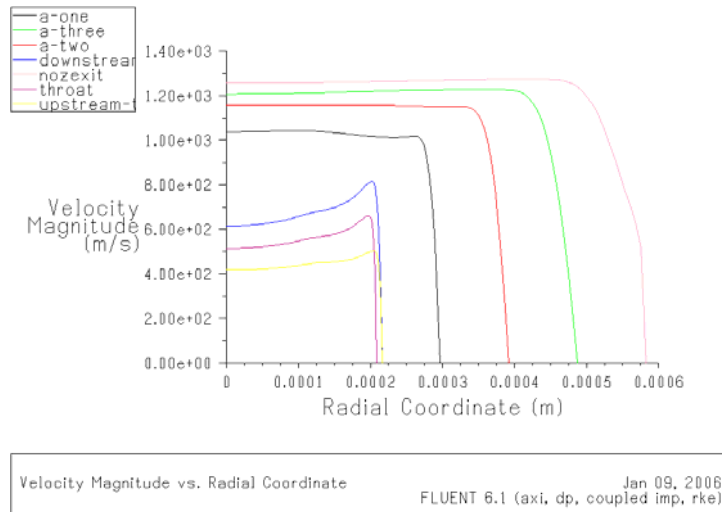


Figure 44: Plot of Velocity Magnitude vs. Radial Coordinate

Alternatively the data may be presented in a chart format, which provides an evaluation of the velocity at predefined locations along the nozzle axis. The position of these locations is shown in Figure 43. The three profiles relating to locations close to the throat exhibit characteristics that are indicative of a distinct boundary layer. The trace increases to a distinct peak velocity before dropping sharply to zero. The peak indicates the edge of the boundary layer, with the sharp decrease in velocity indicating the high velocity gradient within. Each of the traces that correspond to a location further downstream demonstrates a similar general shape, but the peak disappears altogether. This change in the shape of the velocity trace prevents the identification of the edge of the boundary layer as a function of the freestream velocity.

The alternative is to consider the rate of change of axial velocity with respect to radial position. At the edge of the boundary layer velocity of the flow within the boundary layer is the same as the free stream velocity, therefore the rate of change of axial velocity with respect to radial position will be zero. Figure 45 shows contours of the rate of change of axial velocity with respect to the change in radial coordinate. The scale was set to consider any change that was less than zero, indicating deceleration of the flow. The edge of the boundary layer is then clearly visible. The bulges at the exit of the nozzle indicate the rapid change in direction of the flow that occurs at this location. This is illustrated in more detail by Figure 46, which shows the velocity vectors at this point.

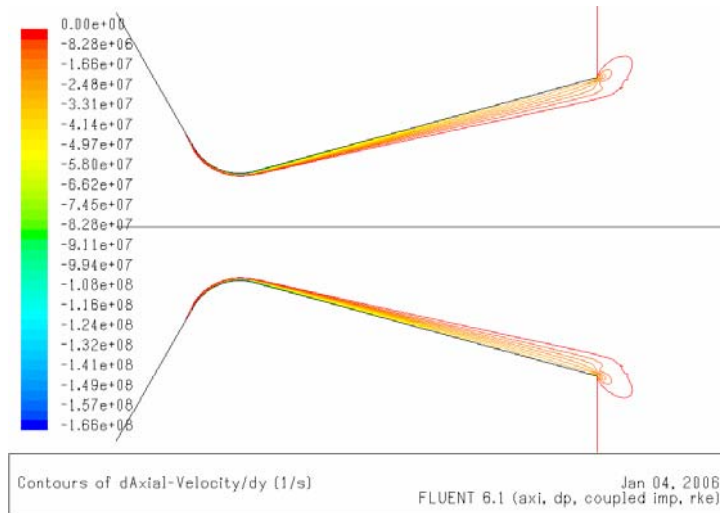


Figure 45: Contours of the Rate of Change of Axial Velocity

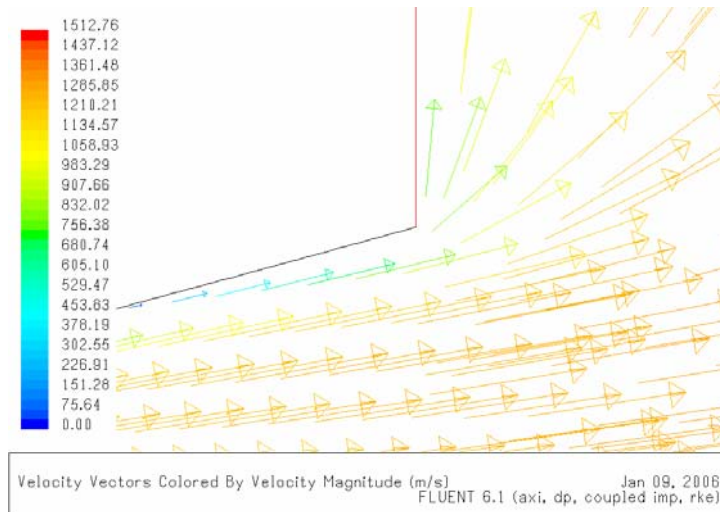


Figure 46: Velocity Vectors at the Nozzle Exit

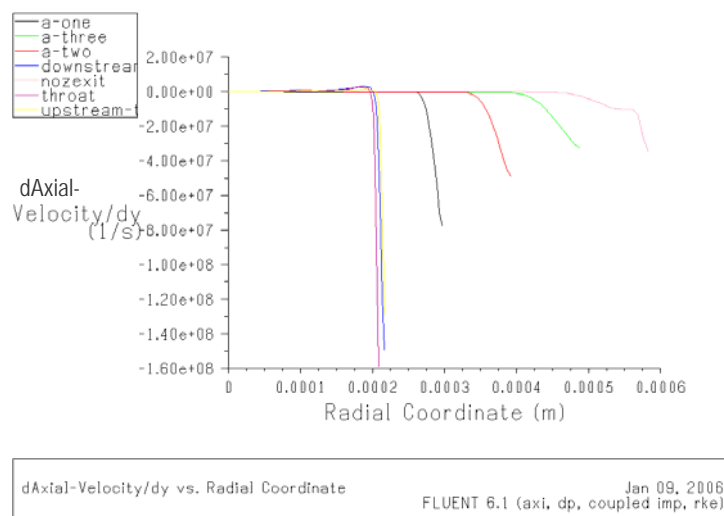


Figure 47: Chart of the Rate of Change of Axial Velocity

The same sample planes that were used previously were used to generate Figure 47. This shows the magnitude of the rate of change of axial velocity with respect to the change in radial coordinate as a function of the radial position. It can be seen that the traces all cross the y-axis at approximately zero thereby indicating that little or no variation is present at the centre line of the nozzle. Each of the traces exhibits similar characteristics, with a period at approximately zero followed by a sharp turn to become negative. The radial coordinate at which this change in direction occurs provides the location of the edge of the boundary layer. The gradient of the trace as it becomes progressively negative is indicative of the intensity of the shear stresses within the boundary layer at that location. In addition in this plot the three traces corresponding to the planes in the vicinity of the nozzle throat indicate an acceleration of the flow, which is to be expected. The trace that relates to the sample plane at the exit from the nozzle, shown in pink exhibits a corner like feature. This corresponds to the bulges noted in Figure 45, which represent the rapid turning of the flow as it exits the nozzle.

Identification of the precise location of the edge of the boundary layer is still difficult from this chart, therefore the data was exported and processed using MS Excel[®]. The results of this will be discussed in more detail in the following section.

4.6 Results and Discussion

Four different nozzle geometries were investigated using numerical modelling. The performance of each type of geometry will be summarised first, followed by a comparison between the different geometries.

4.6.1 Standard Geometry Model Results

Each of the nine thrust levels described was evaluated using the standard geometry model. The results show that as the dimensions of the nozzle reduce, the boundary layer present within the nozzle thickens. The rate at which this occurs also increases with reducing nozzle dimension.

The position of the edge of the boundary layer was evaluated for each model at the seven locations described above. To allow a direct comparison of the thickness of the boundary layer in each case, the position of the edge of the boundary layer was expressed as a function of a non-dimensional radial coordinate. Figure 48 shows the position of edge of the boundary layer at each location described.

The curves shown indicate that the rate at which the boundary layer is developing within the nozzle increases. To evaluate this directly the position of the boundary layer relative to the initial geometry was evaluated and the effective divergence angle was calculated. The effective areas of

the nozzle at the throat and exit plane were then calculated to evaluate the predicted reduction in area due to the presence of a boundary layer.

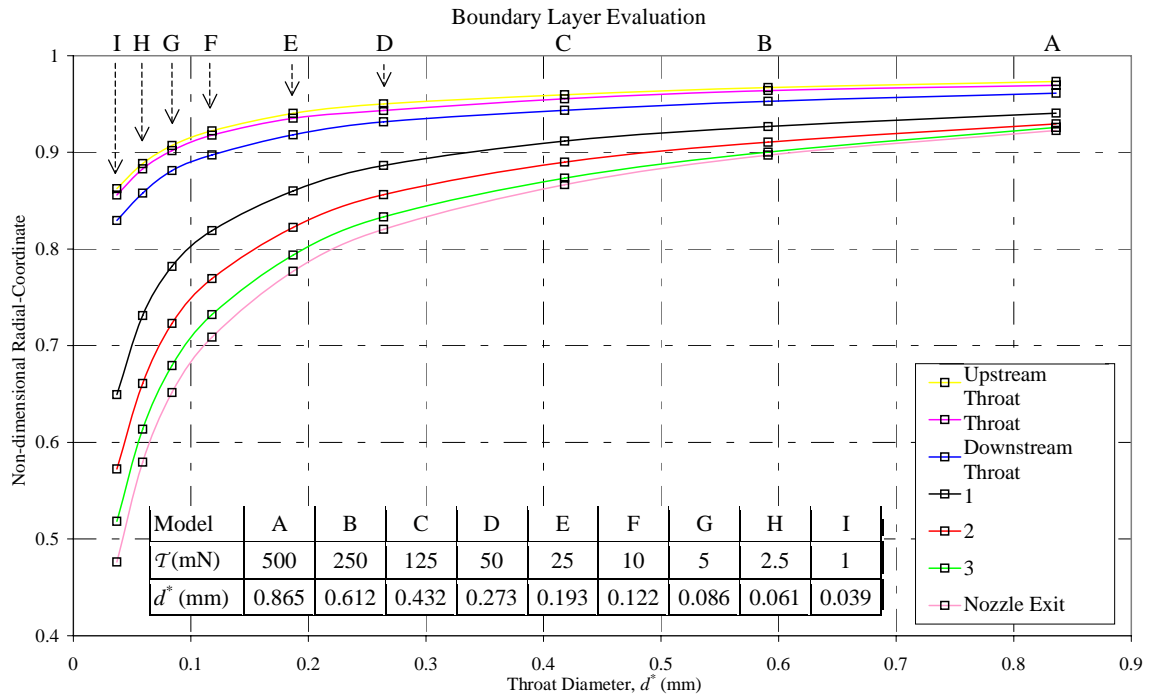


Figure 48: Assessment of the Position of the Edge of the Boundary Layer

In order to evaluate the predicted reduction in c_f the effective exhaust velocity across the exit plane of each nozzle was calculated. This was achieved by using a mass averaged approach to allow for the variation in velocity observed. This, in combination with the value of c^* for each nozzle, allowed the calculation of c_f in each case. The values calculated in each case are given in Table 16.

Model	A	B	C	D	E	F	G	H	I
P_e (Pa)	11889.13	11965.48	11934.63	11987.24	11877.08	11870.98	11936.86	11811.8	11640.48
c_f	1.917	1.908	1.897	1.882	1.874	1.860	1.841	1.822	1.804
c_f - efficiency	93.29%	92.86%	92.32%	91.62%	91.21%	90.54%	89.62%	88.68%	87.82%
T (mN)	500.91	246.43	120.35	46.65	22.81	8.70	4.18	1.97	0.72
T - efficiency	87.67%	86.30%	84.25%	81.87%	79.79%	76.42%	72.88%	69.14%	64.34%
Effective α (°)	13.96	13.32	12.60	11.71	10.66	9.13	8.10	6.52	4.23
% Reduction in A^*	6.02%	7.07%	8.73%	11.02%	12.52%	15.78%	18.68%	22.03%	26.74%
% Reduction in A_e	14.29%	19.52%	24.92%	32.68%	39.62%	49.75%	57.55%	66.42%	77.31%

Table 16: Summary of Data for Standard Geometry Models

The data in Table 16 shows that overall the exit pressure in each case is comparable, indicating a similar level of expansion is achieved. Consideration of the c_f predicted in each case reveals that the performance of the nozzle reduces with decreasing dimension. This is a result of the increasing boundary layer thickness, reducing the throat and exit areas of the nozzle. The c_f efficiency estimate is based upon the ideal value of c_f for these nozzle geometries, which is the same in each case at 2.05. This value assumes perfect expansion and no losses. Inspection of the

c_f efficiency reveals the extent of the reduction in performance in each case, with the smallest nozzle exhibiting the lowest efficiency as expected.

Inspection of the magnitude of thrust predicted reveals that this is also affected by the presence of the thick boundary layer. The thrust efficiency data was calculated using an ideal thrust value in each case, based upon perfect expansion. This data again illustrates that the rate of performance loss increases. Overall this data shows that the trend observed in Figure 48 with respect to the position of the boundary layer is carried forwards into the performance of the nozzle.

The data relating to the expansion half-angle indicates that the boundary layer increasingly fills more of the nozzle, as illustrated by Figure 49. The trend observed exhibits a logarithmic behaviour similar to that shown in Figure 48. The reduction in the expansion half-angle indicates that progressively less expansion of the flow is occurring. In the case of the smallest model, Nozzle I, corresponding to a thrust level of 1 mN, barely any expansion of the flow is observed with an effective expansion angle of 4.23° resulting.

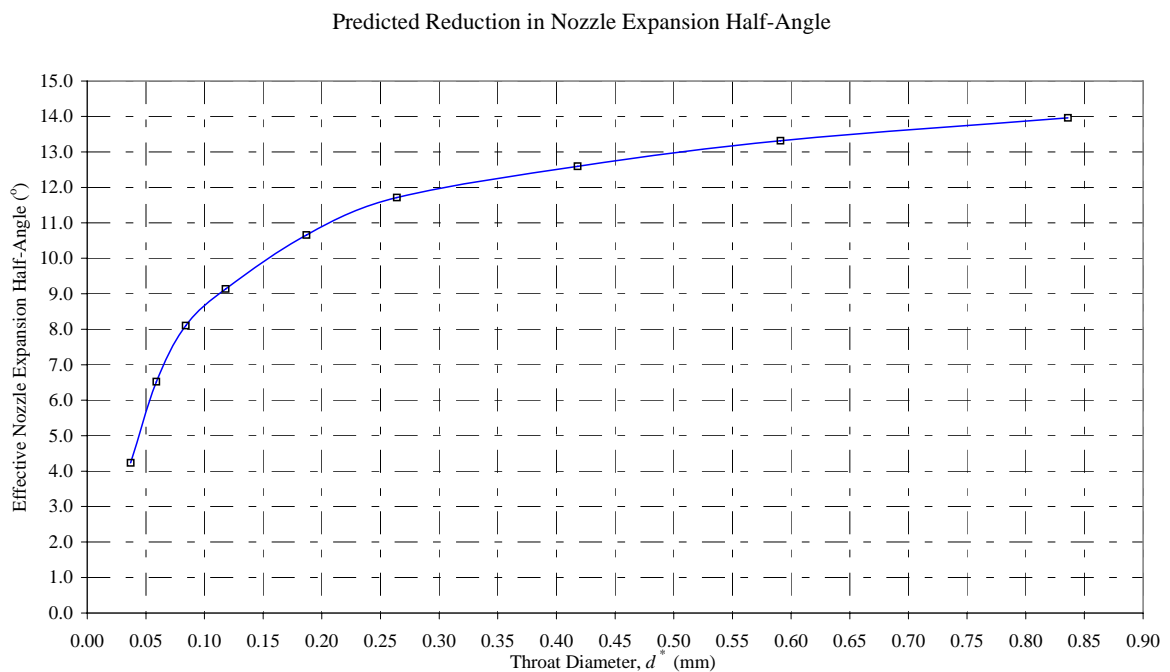


Figure 49: Predicted Reduction in Nozzle Expansion Half-Angle

4.6.2 Wide Expansion Angle Model Results

The results from the standard geometry models indicated that as the dimension of the nozzle reduced further, the effect of the presence of the boundary layer increased. The four models selected for investigation with an increased expansion half angle were A, E, G and I, corresponding to 500, 25, 5 and 1 mN of thrust respectively. It was decided that a cluster of models towards the smaller end of the thrust range investigated would provide the optimal data resolution possible in the time available. A summary of the data generated by these models is

presented in Table 17. Inspection of the exit pressure data reveals that a similar level of expansion is achieved in each case, although the c_f achieved varies significantly. In the case of the largest model, nozzle A, an improvement in both the c_f and T efficiency are achieved in comparison to the standard geometry. As the geometry reduces in size this improvement disappears, with a reduction in performance observed in the other three models.

Model	A	E	G	I
P_e (Pa)	12664.67	12665.63	12102.8	12064.19
c_f	2.01	1.71	1.66	1.60
c_f - efficiency	97.68%	83.44%	80.63%	77.89%
T (mN)	523.15	20.73	3.78	0.64
T - efficiency	91.56%	72.51%	65.56%	57.13%
Effective α ($^\circ$)	19.25	15.03	11.51	7.10
% Reduction in A^*	6.26%	13.10%	18.69%	26.66%
% Reduction in A_e	13.58%	39.57%	57.84%	77.88%

Table 17: Summary of Data for Wide Expansion Angle Models

4.6.3 Sharp Throat Profile Model Results

Figure 45 illustrated the position of the boundary layer in the standard geometry model with reference to contours of the change in axial velocity with respect to radial direction. From this image it is possible to see that the boundary layer begins to develop upstream of the nozzle, approximately at the point where the curvature for the throat of the nozzle begins. To investigate the impact of this on the performance of the nozzle, three models were created with a sharp throat profile. A summary of the data generated by these models is given in Table 18.

Model	A	E	I
P_e (Pa)	12004.86	11958.73	11671.27
c_f	1.915	1.867	1.801
c_f - efficiency	93.22%	90.86%	87.65%
T (mN)	512.16	24.38	0.87
T - efficiency	89.64%	85.27%	78.07%
Effective α ($^\circ$)	13.55	10.18	5.45
% Reduction in A^*	3.84%	6.15%	10.93%
% Reduction in A_e	14.52%	40.60%	71.56%

Table 18: Summary of Data for Sharp Throat Profile Models

The data from these models shows that there is little difference in the performance observed. In general a smooth throat contour is used to provide a slow turning of the exhaust to prevent separation of the flow. If a flow separates within a nozzle a significant reduction in performance is observed. Consideration of the velocity contours from these models reveals that the flow remains attached at all times as shown in Figure 50. The data from the sharp throat models reveals that overall the boundary layer grows at a rate similar to that observed for the standard

geometry case and the c_f predicted is comparable. This indicates that no loss in performance will be observed as a result of the removal of the throat contour.

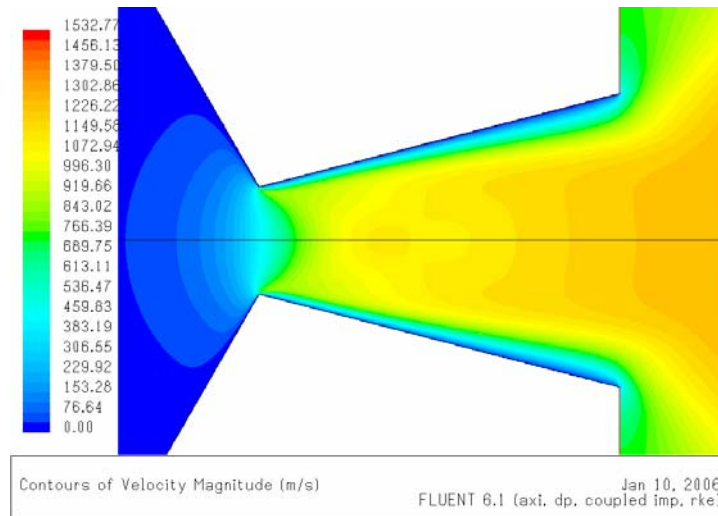


Figure 50: Velocity Contours within a Sharp Throat Profile Model

In terms of the \mathcal{T} predicted, the sharp throat profile produces better results because the boundary layer at the throat is significantly reduced. In addition in the case of the smallest model the thickness of the boundary layer is reduced throughout the nozzle, as illustrated by Figure 51.

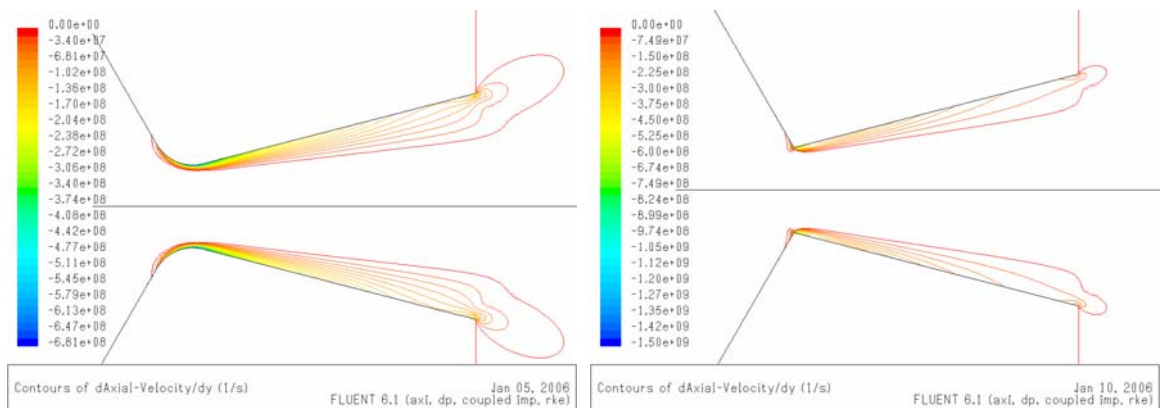


Figure 51: Comparison of Boundary Layer Position

4.6.4 Convergent Section Only Model Results

The final set of models considered the effect on the performance of the thruster if the expanding section of the nozzle was removed completely. Four thrust levels were considered and a summary of the data obtained is presented in Table 19.

From the data presented it is clear that the lack of expansion of the flow would lead to a significant degradation in performance. The c_f and \mathcal{T} predicted in each case are below 50% of the design values, with little variation between the models.

Model	A	E	G	I
P_e (Pa)	311660.2	312001.1	311988.1	311722.4
c_f	0.904	0.880	0.872	0.905
c_f - efficiency	43.98%	42.81%	42.45%	44.06%
\mathcal{T} (mN)	241.79	11.21	2.16	0.41
\mathcal{T} - efficiency	43.98%	42.81%	42.45%	44.06%
% Reduction in A^*	3.78%	8.42%	11.92%	16.39%

Table 19: Summary of Data from Convergent Section Only Models

The reasons for this reduced performance are partially revealed through examination of the velocity vectors at the exit from the model, shown in Figure 52. The image shows how the convergent section of the nozzle accelerates and turns the flow. As the flow exits the nozzle a *vena contracta* appears in the flow, causing the core flow to narrow further and accelerate. Following this the flow quickly diverges and appears to accelerate further due to the vacuum conditions exterior to the nozzle. The rapid divergence of the flow reduces the axial velocity of the flow hence reducing the momentum and thrust of the process. The effect of this may be reduced if an additional straight section were included prior to the flow exit.

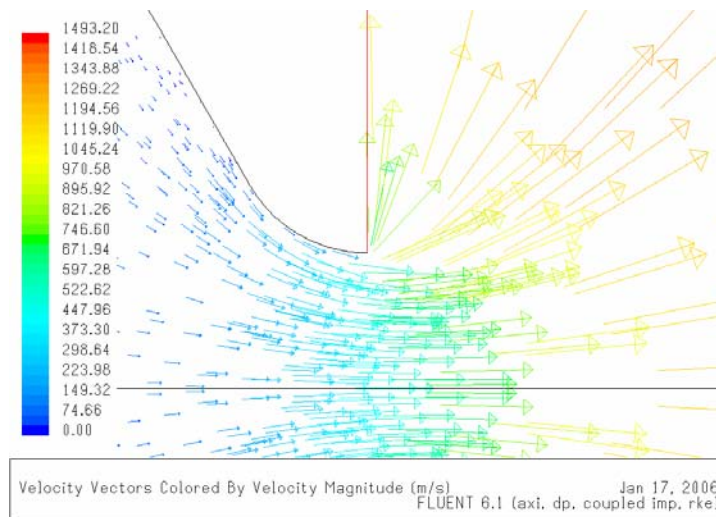


Figure 52: Velocity Vectors at the Exit from a Convergent Section Only Model

4.6.5 Comparison of Results

The data presented has illustrated that significant variations are present in the performance predicted by the various models used. The c_f and \mathcal{T} efficiencies are compared in each case in Figure 53 and Figure 54 respectively.

c_f Efficiency Comparison

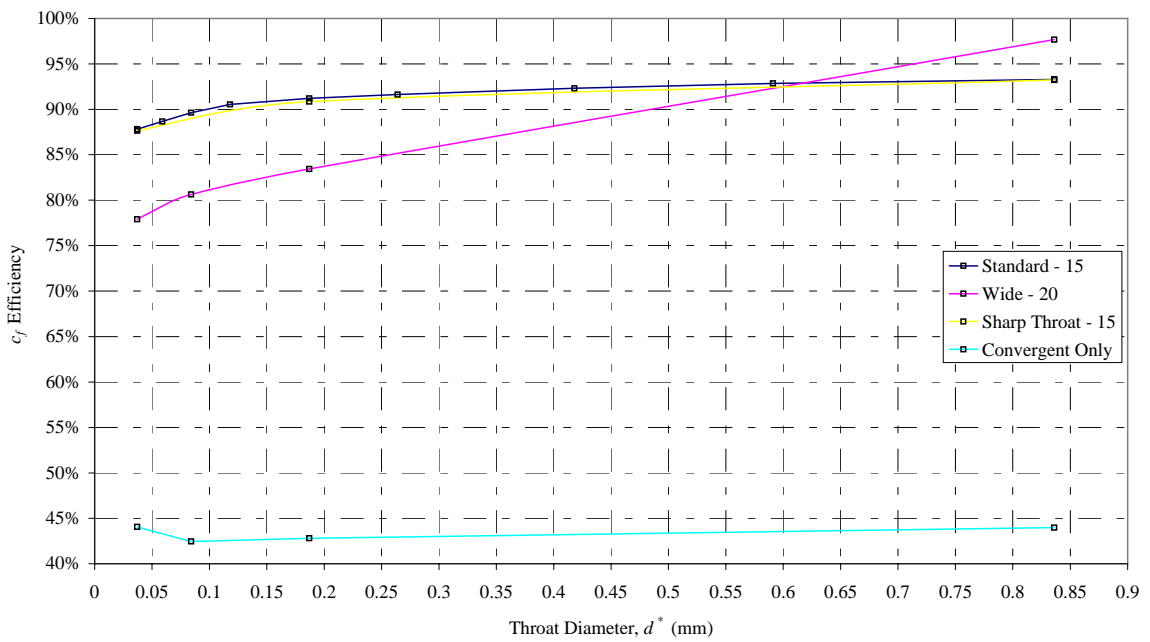


Figure 53: Comparison of c_f Efficiency for the Different Geometries Modelled

Thrust Efficiency Comparison

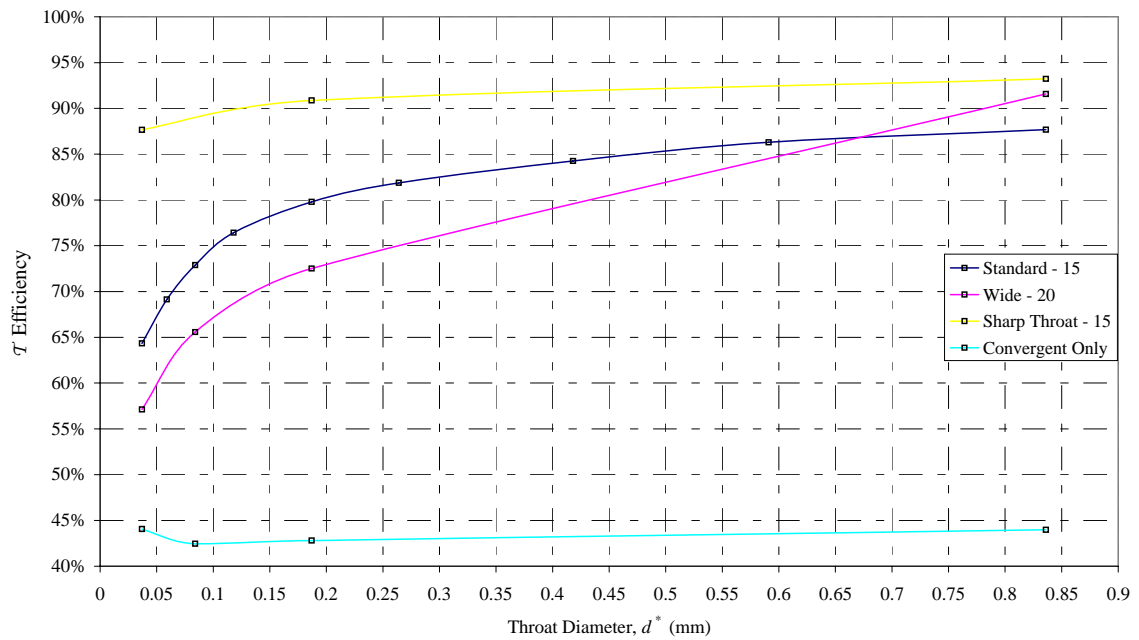


Figure 54: Comparison of Thrust Efficiency for the Different Geometries Modelled

4.7 Conclusions

Through creating and solving a series of models using Fluent[®] the development of a boundary layer within the exhaust nozzle of a hydrogen peroxide thruster has been investigated. The rate of development of the boundary layer has been shown to be logarithmic with a direct impact on the

resultant performance of the nozzle. In the smallest case considered, corresponding to a thrust level of 1 mN, the nozzle divergence half-angle was reduced to 4° due to the presence of a thick boundary layer. The three additional geometries considered in this analysis show that small modifications in the geometry could result in significant changes in performance at small scales. The wide expansion angle model showed performance improvement at large scales, but no improvement at small scales. In addition, the sharp throat model demonstrated that the throat contour is of little concern. The c_f efficiency chart demonstrated that overall there is little difference between the models. In comparison the thrust efficiency chart showed that significant gains were possible through the use of a sharp throat. Finally the models with a convergent section only showed that significant reductions in performance would result if the divergent section were removed altogether.

5 Conclusions

This research aimed to address three key points, relating to propellant decomposition, heat transfer and nozzle flow in a hydrogen peroxide microthruster. The propellant decomposition research has demonstrated that it is possible to reliably decompose hydrogen peroxide in a chamber containing a catalyst of diameter 6.7 mm and length 5 mm. The decomposition temperatures achieved indicate that approximately full decomposition is occurring and tests conducted in ambient temperatures of 0°C confirm cold-start capabilities.

The heat transfer models developed indicated that the insulation of a decomposition chamber is unlikely to reduce thermal losses. The high surface area to volume ratio results in additional radiative losses, therefore it is recommended that a heat shield based design is developed for further testing.

Numerical models were created to investigate the development of a boundary layer within the exhaust nozzle of a hydrogen peroxide thruster. These models revealed that the performance of a nozzle reduces at an increasing rate due to the logarithmic growth of the boundary layer. The presence of a sharp throat contour was found to produce higher thrust levels than a smooth contoured throat at the same divergence angle due to the reduced boundary layer thickness at the throat.

6 Recommendations for Future Work

Overall this research has indicated that it is possible to develop a hydrogen peroxide thruster that will work efficiently at very low thrust levels. Additional testing work with an optimised test setup would allow the presence of pressure oscillations to be investigated further and removed from the decomposition characteristic. The installation of a heat shield would further improve the temperature profile through the reduction of radiative losses.

In addition further development of the numerical models relating to nozzle geometry would enable the results generated to be further developed.

7 Bibliography

- [Atkins'97] ATKINS, P. & JONES, L. (1997) *Chemistry: Molecules, Matter and Change*, Freeman.
- [Davis'60] DAVIS, N. S. & MCCORMICK, J. C. (1960) Design of Catalyst Packs for the Decomposition of Hydrogen Peroxide. IN BOLLINGER, L. E., GOLDSMITH M., LEMMONS, JR. A. W., (Ed.) *Liquid Rockets and Propellants*. New York, NY, Academic Press.
- [Eloiri'01] ELOIRDI, R., *et al* (2001) An Investigation of Various Catalysts in a Small Hydrogen Peroxide Thruster. *1st International Conference on Green Propellants for Space Propulsion*. ESTEC, Noordwijk, NL, ESA.
- [Hill'92] HILL, P. G. & PETERSON, C. R. (1992) *Mechanics and Thermodynamics of Propulsion*, Addison-Wesley.
- [Hsieh'04] HSIEH, S., *et al* (2004) Liquid Flow in a Micro-Channel. *Journal of Micromechanics and Microengineering*, 14, 436-445.
- [Ivanova'02] IVANOVA, N. D., *et al* (2002) High-Performance Manganese Oxide Catalysts for CO Oxidation. *Russian Journal of Applied Chemistry*, 75, 1420-1423.
- [Kappenstein'05] KAPPENSTEIN, C., *et al* (2005) Chemical Micropropulsion: State of the Art and Catalyst Surface Requirements. *41st AIAA/ASME/SAE/ASEE Joint Propulsion Conference & Exhibit*. Tucson, AZ, AIAA.
- [Mala'99] MALA, G. M. & LI, D. (1999) Flow Characteristics of Water in Microtubes. *International Journal of Heat and Fluid Flow*, 20, 142-148.
- [Richardson'00] RICHARDSON, J. T., *et al* (2000) Properties of Ceramic Foam Catalyst Supports: Pressure Drop. *Applied Catalysis A: General*, 204, 19-32.
- [Schlichting'00] SCHLICHTING, H. & GERSTEN, K. (2000) *Boundary Layer Theory*, Springer.
- [Smith'04] SMITH, R. T. & SAMBROOK, R. M. (2004) Production of Porous Articles. Dytech Corporation Ltd, Sheffield, GB.
- [Sutton'01] SUTTON, G. P. & BIBLARZ, O. (2001) *Rocket Propulsion Elements*, Wiley - Interscience.
- [Willis'60] WILLIS, C. M. (1960) The Effect of Catalyst-Bed Arrangement on Thrust Buildup and Decay Time for a 90% Hydrogen Peroxide Control Rocket. NASA.